

# Mitochondrial damage in muscle specific PolG mutant mice activates the integrated stress response and disrupts the mitochondrial folate cycle

---

Received: 23 June 2024

---

Accepted: 13 February 2025


---

Published online: 08 March 2025

---

 Check for updates

---

Simon T. Bond <sup>1,2,3,11</sup>, Emily J. King <sup>1,3,11</sup>, Shannen M. Walker <sup>1,3</sup>, Christine Yang<sup>1</sup>, Yingying Liu<sup>1</sup>, Kevin H. Liu<sup>1</sup>, Aowen Zhuang<sup>1</sup>, Aaron W. Jurrjens <sup>1,3</sup>, Haoyun A. Fang<sup>1</sup>, Luke E. Formosa <sup>4</sup>, Artika P. Nath<sup>1</sup>, Sergio Ruiz Carmona <sup>1</sup>, Michael Inouye<sup>1</sup>, Thy Duong <sup>1</sup>, Kevin Huynh <sup>1,2</sup>, Peter J. Meikle <sup>1,2,3,5</sup>, Simon Crawford<sup>6</sup>, Georg Ramm <sup>4,6</sup>, Sheik Nadeem Elahee Doomun <sup>7</sup>, David P. de Souza<sup>7</sup>, Danielle L. Rudler<sup>8,9</sup>, Anna C. Calkin <sup>1,2</sup>, Aleksandra Filipovska <sup>8,9</sup>, David W. Greening <sup>1,2,3,5</sup>, Darren C. Henstridge <sup>1,10</sup> & Brian G. Drew <sup>1,2,3,5</sup> 

During mitochondrial damage, information is relayed between the mitochondria and nucleus to coordinate precise responses to preserve cellular health. One such pathway is the mitochondrial integrated stress response (mtISR), which is known to be activated by mitochondrial DNA (mtDNA) damage. However, the causal molecular signals responsible for activation of the mtISR remain mostly unknown. A gene often associated with mtDNA mutations/deletions is *Polg1*, which encodes the mitochondrial DNA Polymerase  $\gamma$  (PolG). Here, we describe an inducible, tissue specific model of PolG mutation, which in muscle specific animals leads to rapid development of mitochondrial dysfunction and muscular degeneration in male animals from ~5 months of age. Detailed molecular profiling demonstrated robust activation of the mtISR in muscles from these animals. This was accompanied by striking alterations to enzymes in the mitochondrial folate cycle that was likely driven by a specific depletion in the folate cycle metabolite 5,10 methenyl-THF, strongly implying imbalanced folate intermediates as a previously unrecognised pathology linking the mtISR and mitochondrial disease.

Mitochondria are small, double membraned organelles found in most eukaryotic cells, often in their thousands. Their cellular roles include the regulation of several processes including apoptosis, redox balance, inflammation and ATP production. Mitochondria are unique in that they harbour their own genome (mtDNA), which is small and circular, and encodes for 37 of the ~1500 genes required for efficient mitochondrial function<sup>1–3</sup>. Of the 37 genes, 22 are transfer RNAs (tRNA), 2

are mitochondrial ribosomal RNAs (rRNA), and 13 are protein coding genes critical for optimised functioning of the mitochondrial electron transport chain (ETC)<sup>4–7</sup>. The remainder of the ~1500 required mitochondrial proteins are transcribed by the nuclear genome, translated in the cytosol, then imported into the mitochondria. Each mitochondrion can harbour several copies of mtDNA, where it is replicated and maintained by dedicated transcriptional machinery including

---

A full list of affiliations appears at the end of the paper. ✉ e-mail: [brian.drew@baker.edu.au](mailto:brian.drew@baker.edu.au)

Mitochondrial transcription factor A (TFAM), DNA polymerase gamma (PolG), helicase Twinkle (TWNK), Mitochondrial single-strand binding protein (SSBP1) and Mitochondrial RNA polymerase (POLRMT)<sup>7</sup>. PolG is proposed to be the sole DNA polymerase found in the mitochondria and is essential for the replication and maintenance of mtDNA<sup>8</sup>. The mature PolG enzyme consists of three components: the catalytic PolG1 protein, and two units of the accessory subunit PolG2. The PolG enzyme has three main enzymatic actions; DNA polymerase activity, DNA exonuclease activity (proofreading), and base excision repair<sup>9</sup>.

Mutations to mtDNA are often a cause of mitochondrial dysfunction and subsequent mitochondrial disease (MD)<sup>10</sup>. Indeed, the most common genetic cause leading to an increase in mtDNA mutations, is coding mutants in the *Polg1* gene<sup>11</sup>. *Polg1* mutations can, amongst other defects, lead to a dysfunctional PolG enzyme complex that lacks the ability to efficiently replicate or proofread mtDNA, ultimately leading to an accumulation of mtDNA mutations/deletions, mtDNA depletion and subsequent mitochondrial dysfunction<sup>11–13</sup>. PolG induced diseases vary dramatically in their presentation, and often develop unpredictably from birth through to later life. PolG pathologies are various in their presentation and lead to degenerative muscle, neurological and metabolic diseases<sup>12–16</sup>. PolG induced mtDNA mutations/deletions mostly occur randomly across the mitochondrial genome, although the major arc (between the two origins of replication) attracts a major part of this mutational burden<sup>17,18</sup>. Often, the location of the mutation is unrelated to the development of clinical symptoms, where instead it is the burden of overall mutational load in a given tissue/cell that is the pathological switch<sup>19,20</sup>. Cells that harbour both WT and mutant variants of mtDNA are described as being heteroplasmic, where the cell can maintain mostly normal function so long as the ratio of mutant versus WT copies remains below a given threshold<sup>21</sup>. However, once the ratio exceeds that threshold, disease pathologies rapidly develop<sup>19–21</sup>.

Much of our prior understanding of the mechanisms underlying PolG mediated disease has been generated from human studies in individuals carrying SNPs in the *Polg1* coding sequence, and from mouse models that harbour a whole body insufficiency in PolG exonuclease activity, known as the mitochondrial mutator mouse - of which two independent models currently exist<sup>12,13</sup>. These transgenic mice were generated by base substitution of an aspartate to alanine residue at site 257 (D257A) of the PolG protein, which falls within the conserved exonuclease domain. The D257A Mutator mice subsequently lack PolG exonuclease activity and thus accumulate mtDNA mutations over time<sup>12,13</sup>. Homozygous D257A PolG mice present with multiple disorders by early adulthood including the progressive loss of body mass, skeletal muscle and bone mass, amongst other ailments such as cardiomyopathy, premature aging, kyphosis, impaired mobility and ultimately premature death<sup>11–14,22</sup>. As expected, the organs most affected in these mice are those that are heavily reliant on mitochondrial energy production such as the brain, muscle and heart. However, the temporal and tissue-specific aspects of disease progression in the mutator mouse has been difficult to dissect due to its developmental nature. For example, with the described heart failure that develops in these mice<sup>23</sup>, it is difficult to determine how much of this pathology is due to intrinsic mitochondrial defects in cardiomyocytes, compared to systemic issues relating to metabolic dysregulation, neurological degeneration and skeletal muscle atrophy. Given this predicament, it is important to advance our understanding of how increasing mtDNA mutation load affects these tissues individually, and how this subsequently drives complications.

Herein, we describe a conditional mouse model that allows for specific removal of the PolG exonuclease domain, resulting in tissues that express a truncated PolG protein with all elements of function intact—other than the proof-reading/repair capacity. This mouse can be crossed with cre-recombinase expressing mice to generate models with tissue-specific manipulation of PolG activity.

In the current study we investigated an inducible, post-developmental skeletal muscle specific model (ACTA1-cre-ERT2), which presented with a systemic phenotype from ~5 months post-recombination. Importantly, not all features of the whole body PolG mutator mouse are recapitulated in our model, suggesting that many of the features observed in the global mutator mouse either arise from developmental defects, differential aetiology, or from tissue crosstalk arising from mitochondrial dysfunction in other tissues. Importantly, we also use this mouse to reveal fundamental insights into our understanding of the mitochondrial integrated stress response (mtISR), where evidence presented herein suggests that mtDNA deletions induced by PolG dysfunction, lead to alterations in the mitochondrial folate cycle which likely contribute to the chronic activation of the mtISR pathway.

## Results

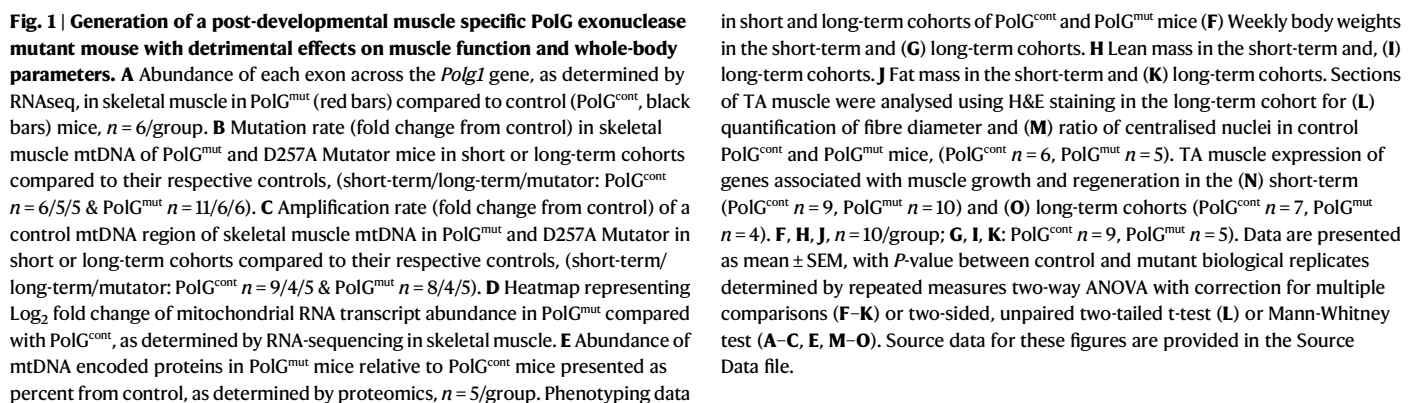
### Generation and validation of a muscle specific PolG exonuclease mutant

In this study, we sought to develop a Cre-Lox mediated mouse model which allowed for temporal and tissue specific manipulation of PolG exonuclease (DNA proofreading) activity. We aimed to specifically interrupt PolG exonuclease activity to induce mtDNA damage (deletions/mutations), which is often the prevailing insult leading to disease phenotypes in a high proportion of humans who have pathogenic polymorphisms in the PolG gene.

To generate this unique mutant, we flanked exons 4 and 5 of the *Polg1* gene with LoxP sites using CRISPR and cross-bred mutant mice with wildtype C57BL/6J mice for 5 generations, before crossing to Cre-recombinase expressing mice. In this study we chose to investigate the impact of PolG exonuclease deletion in skeletal muscle using the ACTA1-cre-ERT2 mouse (Supplementary Fig. 1A). This model allowed for temporal and skeletal muscle specific deletion of PolG exonuclease activity via Tamoxifen induced Cre-activation. We focussed on skeletal muscle due to the previously described degenerative phenotype (ragged red fibres) observed in global PolG mutator (PolG D257A transgenic) mice<sup>16</sup>, and the prominent role that skeletal muscle plays in mitochondrial disease phenotypes. Two groups of mice (fl/fl and fl/fl-Cre) were generated that were further divided into groups that either received Tamoxifen (80 mg/kg) in oil, or oil alone; fl/fl-OIL, fl/fl-TAM (PolG<sup>cont</sup>), fl/fl-cre-OIL and fl/fl-Cre-TAM (PolG<sup>mut</sup>) (Supplementary Fig. 1B). Cohorts were then studied for two different time periods: 4 months (referred to from this point as “short-term”) and 12 months (referred to from this point as “long-term”).

Given that this was the first model generated using this conditional PolG exonuclease mutant mouse, we sought to test key aspects to confirm its validity. We first set out to demonstrate that skeletal muscle specific deletion of exon 4 and 5 was successful, and that this did not result in complete loss of PolG mRNA due to non-sense mediated decay. Using RNA-sequencing data we demonstrate robust reductions (Log<sub>2</sub> fold = -4; -12–16 fold) in counts across both exons 4 and 5 of the PolG mRNA transcript in muscle from PolG<sup>mut</sup> mice, with no evidence of reduction in other exons (Fig. 1A). Using qPCR, we show that a significant reduction in exon 4–5 abundance was only observed in the skeletal muscle of PolG<sup>mut</sup> mice, and not in other tissues including heart and white adipose tissue (Supplementary Fig. 1C). Together, these data provide evidence that the PolG mRNA transcript in mutant mice is deleted for exons 4 and 5 in skeletal muscle, but retains all other exons and components.

We next wanted to establish that the truncated PolG mRNA transcript could indeed generate a protein product. To do this we performed mass spectrometry proteomics on isolated mitochondria from tibialis anterior (TA) muscles to determine PolG abundance in control and mutant muscle. These data demonstrated an ~50% ( $p < 0.0079$ ) decrease in PolG abundance (relative to PolG<sup>cont</sup> mice,  $n = 5$ ) (Supplementary Fig. 1D), confirming that our mouse model does



slightly elevated in PolG<sup>mut</sup> muscle, whilst TFAM was notably reduced (Supplementary Figs. 1E and F). We also quantified the abundance of mtDNA in whole muscle from PolG<sup>mut</sup> and PolG<sup>cont</sup> mice at 12 months of age, alongside heterozygous 12 month old mice from the previously described global D257A PolG mutator mouse (which does not have a major replication deficit)<sup>12</sup>. These data confirm that both models demonstrated the same partly reduced mtDNA abundance compared to control mice (Supplementary Fig. 1G), implying that our skeletal muscle specific PolG<sup>mut</sup> model behaved similarly with regards to mtDNA replication to the well described global PolG mutator model.

Another important validation of this model was to determine whether removal of the exonuclease domain led to alterations in the integrity of mtDNA (mutations/deletions) in skeletal muscle. To investigate this we performed the Random Mutation Capture (RMC) assay<sup>24</sup>, coupled with droplet digital PCR (ddPCR) which together can be used to estimate mutation and deletion frequency<sup>24</sup> in the mtDNA. As a positive control for this assay, we used mtDNA isolated from muscle of the global PolG mutator (D257A) mouse, which has previously been shown to display substantially increased mutations and deletions in mtDNA<sup>24</sup>. Using these assays we observed a higher level of mutations isolated from global PolG Mutator muscles, compared to aged match control samples (Fig. 1B – purple bar). Interestingly however, from our PolG<sup>mut</sup> muscle we did not observe any difference in the mutation load of mtDNA, in samples from either short- or long-term muscle specific PolG<sup>mut</sup> mice (Fig. 1B – red and blue bars respectively). Given this result, we next sought to test the deletion frequency in the mtDNA. When we performed amplification abundance assays in equivalent amounts of mtDNA from WT and global PolG Mutator muscle, we noted that there was a minor non-significant reduction in the amplification in Mutator muscles, indicating some deletions (and thus loss of signal) were occurring (Fig. 1C – purple bars). However, when we performed the same analysis in mtDNA from our PolG<sup>mut</sup> muscles, we observed a significant reduction in amplification in both short and long term muscles compared to PolG<sup>cont</sup> muscle (Fig. 1C – red and blue bars), suggesting that more than half of the mtDNA molecules in the PolG<sup>mut</sup> muscles harboured deletions. Consistent with this finding, when we used conventional PCR to amplify a 10 kb section of mtDNA from these same samples which is prone to deletion, we observed amplicons of many various sizes (smears) in PolG<sup>mut</sup> mtDNA, compared to a mostly single consistent amplicon of 10 kb in PolG<sup>cont</sup> mtDNA (Supplementary Fig. 1H). Taken together, these findings provide strong evidence that mtDNA from PolG<sup>mut</sup> muscles are truncated, with the presence of mtDNA deletions, confirming a pathological molecular consequence related to our muscle specific PolG mutant model.

Lastly, given that an additional function of PolG relates to its role in facilitating mtDNA transcription we sought to investigate mitochondrial transcriptional activity in our model. We therefore performed a bespoke RNA-sequencing analysis to assess global mitochondrial transcription, as previously described<sup>25</sup>. Our data demonstrate that contrary to a reduction in mtDNA transcription, we observed a robust global increase in expression of all mitochondrial encoded mRNAs (Fig. 1D) in our mutant muscle. This was universal across both the positive and negative mtDNA strands in PolG<sup>mut</sup> muscles compared to control (range from 0.5–3 Log<sub>2</sub> fold increase) (Supplementary Figs. 1I and J). Thus, these data provide evidence that there is no impairment in mtDNA transcription in our mutant PolG model. Interestingly, whilst mitochondrial transcription was increased in the mutant muscles, analysis of mtDNA encoded protein abundance using mass spectrometry appeared to be mostly reduced (Fig. 1E), indicating a potential defect in mitochondrial protein translation—a phenomenon that is investigated in more detail later in the manuscript.

Overall, in the above studies we provide strong evidence that we have indeed generated a muscle specific PolG mutant model, and not a KO model. The inducible muscle specific PolG<sup>mut</sup> model does not substantially negatively impact mtDNA replication, mtDNA transcription, or the abundance of proteins important in maintaining mtDNA integrity. It does however lead to impairments in mtDNA integrity, specifically through a demonstrated increase in mtDNA deletions.

### Health impacts of muscle specific loss of PolG exonuclease activity

After validating that our model displayed the molecular characteristics of a muscle specific model of mtDNA deletions, we next investigated what impact this pathology had on whole body health, metabolism and

physiology. The first and possibly most striking observation noted in these animals, was a robust and rapid loss of body weight starting at ~4 months (16 weeks) post-induction (tamoxifen). This was evident late in the short-term cohort (Fig. 1F), but was most prominent and robust in the long-term cohort (Fig. 1G). In these older mice, weight loss started from ~4 months (16 weeks) post-tamoxifen, and mostly persisted until the end of the study. This occurred only in the PolG<sup>mut</sup> mice, and not in any of the other three control lines at any time point (Supplementary Figs. 2A and B). Using EchoMRI, we demonstrate that over the period of the long term cohort, but not the short term, there was a significant reduction in lean mass (Fig. 1H, Supplementary Fig. 2C), with the greatest reduction at 32 weeks (Figs. 1I and Supplementary Fig. 2D). The biggest contributor to overall weight loss in these animals was reduced fat mass, which was significantly lower in the shorter term cohort at the end of the study (Fig. 1J), where the longer term cohort of mice had lost approximately half of their fat mass by 32 weeks post-tamoxifen, compared to controls (Figs. 1K, Supplementary Fig. 2E and F), indicating a specific reduction in adiposity in these animals. The loss of lean mass did not impact isolated muscle weights in the short-term cohort (Supplementary Fig. 2G), however muscles were smaller in the longer term mutant mice with a significant reduction in muscle weights observed for TA, Extensor digitorum longus (EDL) and gastrocnemius (Gastroc) at 12 months of age (Supplementary Fig. 2H). Importantly, this loss in tissue weight was not observed for other organs in these animals including heart and liver for either the short- or long-term cohorts (Supplementary Fig. 2I and J), indicating that these animals were not just smaller per se.

Given the prominent reduction in muscle weights in aged animals, we suspected that the muscle specific PolG mutant was likely inducing a muscle degenerative phenotype, consistent with many models in which mtDNA and mitochondrial function have been disrupted in myofibres<sup>26–28</sup>. Indeed, photographs taken of the animals at the end of the long term study (Supplementary Fig. 2K) showed that the PolG<sup>mut</sup> mice were smaller and less muscular than control mice, with kyphosis (curved spine, white arrow) being present in some animals, consistent with musculo-degenerative phenotypes. To investigate the potential for a musculo-degenerative phenotype in more detail, we analysed histological sections of TA muscle (Supplementary Fig. 3A), where we observed a reduction in fibre diameter (Fig. 1L), change in fibre size distribution in PolG<sup>mut</sup> muscle (Supplementary Fig. 3B), and a greater proportion of fibres by histology that displayed centralised nuclei (Fig. 1M and white arrows in Supplementary Fig. 3A), the latter of which is an indicator of new and regenerating fibres. Functionally, this remodelling and subsequent reduction in muscle mass, led to an overall loss of muscular endurance, as evidenced by a reduced latency to fall-time using the forearm hang wire test (Supplementary Fig. 3C), which was most evident at 24 and 36 weeks post-tamoxifen. PolG<sup>mut</sup> mice also exhibited postural and gait deficiencies compared with PolG<sup>cont</sup> mice, as assessed by DigiGait analyses (Supplementary Figs. 3D–I) including altered paw area, reduced walking acceleration/deceleration (minimum and maximum dA/Dt) and alterations in gait (overlap distance) at 33 weeks of age. Lastly, as a final analysis on the muscle degenerative phenotype, we used qPCR to investigate transcriptional pathways in the skeletal muscle that would support these findings. Indeed, we observed a moderate reduction in mature muscle markers in the short-term cohort mice, with a reciprocal upregulation of Myogenin (*MyoG*), an early myogenesis marker (Fig. 1N). The regenerative phenotype was more substantial in older mice, with robust upregulation of several markers of new fibre formation and myogenesis including *MyoG*, *Myh3*, *Myh8* and *Tnni1* (Fig. 1O).

### Metabolic impacts of muscle specific loss of PolG exonuclease activity

Our data above indicate that as PolG<sup>mut</sup> mice age, their skeletal muscle is subjected to specific insults that lead to a degenerative phenotype



and overall loss of muscle function and endurance. Such impacts would explain why muscle mass in these mice was smaller and animals more frail, but are unlikely to explain why the animals had such profound changes in fat mass. Interestingly, this is not due to major changes in food intake in these animals (Supplementary Fig. 3J and K), and therefore subsequent investigations focussed on what molecular underpinnings might lead to these systemic impacts on metabolism.

To understand this further, we investigated whole body energy expenditure and glucose tolerance. Using the Promethion Metabolic Cage system we could not detect any major differences in Respiratory Exchange Ratio (RER) in the shorter term cohorts (where body weights were mostly equivalent) (Supplementary Figs. 4A and B), or changes in movement (Supplementary Fig. 4C). In long-term cohorts of PolG<sup>mut</sup> mice, we detected a minor (not significant) elevation in RER in the night period (Supplementary Figs. 4D and E), but no differences in overall movement (Supplementary Fig. 4F). Similarly, in short term mice we also observed no detectable differences in Energy Expenditure (EE) between PolG<sup>mut</sup> and PolG<sup>cont</sup> mice (Supplementary Figs. 4G and H). Notably, EE was significantly reduced in PolG<sup>mut</sup> mice in the long term cohort of animals, which was consistent across both the day and night periods (Supplementary Figs. 4J and K), likely reflecting the reductions in body weight at this age. To test for this specifically, we performed ANCOVA analysis, where we observed no difference in EE in both young and older animals (Supplementary Figs. 4I and L, respectively), strongly suggesting that the EE differences observed in the older PolG<sup>mut</sup> mice was due to differences in body weight. We also performed oral glucose tolerance tests (oGTT), which demonstrated that younger cohorts had no difference in glucose tolerance (Supplementary Fig. 5A), whereas the long term cohort of mice PolG<sup>mut</sup> animals displayed a significantly improved glucose tolerance (Supplementary Fig. 5B). We also measured plasma insulin at the 0 and 15 minute time point post-glucose during the GTTs in both young and aged mice, and demonstrated that insulin was significantly reduced 15 minutes post-glucose in PolG<sup>mut</sup> mice in both cohorts compared with PolG<sup>cont</sup> (Supplementary Figs. 5C and D), suggesting improved insulin sensitivity in PolG<sup>mut</sup> mice, consistent with a reduced adiposity.

Overall, in the context of food intake and EE data, the above findings indicate that the large differences in fat mass between PolG<sup>mut</sup> and PolG<sup>cont</sup> mice, led to measurable improvements in whole body glucose tolerance and likely insulin sensitivity, which was most obvious in older mice.

### Mitochondrial-centric changes induced by muscle specific loss of PolG exonuclease activity

With animal phenotyping data demonstrating major changes in body composition and reduced fat mass, we were interested in understanding what changes might be occurring intrinsically to mitochondria, to explain such outcomes. Firstly, to investigate at a morphological and structural level that there were indeed alterations to mitochondrial networks and integrity, we performed STEM imaging of muscles from control and mutant mice (Supplementary Fig. 6). These data demonstrate major disruptions to mitochondrial ultrastructure, morphology and networking within aged muscles of mutant mice, with evidence of expansion in sarcoplasmic reticulum (SR) mass and the appearance of small vesicles resembling autophagosomes. This was accompanied by obvious reorganisation of the muscle ultrastructure, with disruptions to z-line symmetry, filament swelling and reductions in I-band width. To investigate this at the molecular level, we performed proteomics on isolated intact mitochondria from quadriceps muscles from the short term PolG<sup>mut</sup> and PolG<sup>cont</sup> mice<sup>29</sup> ( $n = 8/\text{group}$ ), to understand proteomic changes occurring prior to changes in body composition. This resulted in the quantification of 2275 proteins in total; 1319 proteins in the PolG<sup>cont</sup> mitochondria, and 1353 proteins in PolG<sup>mut</sup> mitochondria, which collectively covered 795/1140 of the known mitochondrial proteome (Supplementary Fig. 7A

and Supplementary Data 1) as previously described in MITOcarta 3.0<sup>30</sup>. Hierarchical clustering of differentially regulated proteins demonstrated that the proteins which were altered, were consistent amongst individual samples of each genotype, and in some instances were different in their z-score by up to 6 z-score units (Fig. 2A). Principle Component Analysis (PCA) demonstrated that we were able to statistically separate the genotypes (Fig. 2B). Differential expression data (Fig. 2C) identified 68 proteins upregulated (red dots) in PolG<sup>mut</sup> mitochondria, and 142 downregulated (blue dots). The top 20 most significantly regulated proteins revealed key members of pathways such as ETC activity, mitochondrial ribosome function and mitochondrial folate cycle (Supplementary Fig. 7B). Pathway enrichment analysis demonstrated highly significant ( $q < 1e^{-30}$ ) enrichments in downregulated pathways associated with “mitochondrial respiratory chain”, “mitochondrial electron transport” and “mitochondrial ATP synthesis” (Fig. 2D). Regarding upregulated pathways, we observed less significant though broader enrichments, with the strongest being observed in pathways associated with alternative metabolism and metabolic processes (carboxylic acid, proline metabolism, amino acid catabolism), as well as protein import and cellular stress responses. As a way of highlighting the strongest enrichments, we plotted individual proteins from two of the most regulated pathways (mitochondria respiratory chain complexes, mitochondrial transcription/ribosome) which demonstrated striking consistency in the downregulation of the vast majority of proteins associated with specific ETC complexes, including Complex I, III and IV (Fig. 2E), and in proteins involved with mitochondrial ribosome/protein translation (Fig. 2F).

The specific changes in individual ETC complexes was consistent with data from previous studies that have investigated models in which mtDNA machinery is disrupted<sup>31</sup>. Complex I is a primary component of the electron transport system and its dysfunction is often linked to degenerative diseases<sup>32–36</sup>. We showed using Blue Native PAGE (BN-PAGE) analysis in PolG<sup>cont</sup> versus PolG<sup>mut</sup> muscle that mature Complex I (~980 kDa) was lower in PolG<sup>mut</sup> muscle compared to PolG<sup>cont</sup> muscle, and consistent with proteomics data, mature Complex II formation appeared to be unaffected (Fig. 2G). Quantitation of the ratio of CI/CII confirmed a significant ~30% reduction in mature Complex I abundance (Fig. 2H), providing evidence that there may be reduced Complex I activity in PolG<sup>mut</sup> skeletal muscle. In order to functionally test the activity of individual ETC components, we analysed isolated mitochondria from skeletal muscle (TA) of PolG<sup>mut</sup> mice using the Seahorse XFe96 Flux analyser. Data from both short and long-term cohorts demonstrated that there was no significant impairment in oxygen consumption rate (OCR) mediated by any ETC components in the young PolG<sup>mut</sup> mitochondria (Fig. 2I, J), but there was a reduction in OCR driven by Complex I in the mitochondria isolated from older PolG<sup>mut</sup> mice (Fig. 2K, L).

Consistent with changes in mitochondrial function and remodelling, we identified a major remodelling in abundance of cardiolipin (CL) species between PolG<sup>cont</sup> and PolG<sup>mut</sup> TA muscles using targeted lipidomics analysis (Supplementary Data 2). Specifically, we identified an overall increase in CL precursor lipids; phosphatidylglycerols (PG) (Fig. 2M), as well as an increase in the total abundance of CLs in PolG<sup>mut</sup> TA muscles (Fig. 2N). CLs are a critical lipid found in the inner mitochondrial membrane that usually contain two Phosphatidic Acid (PA) groups (each containing two FAs acyl chains), and thus these changes are likely associated with major mitochondrial remodelling, as previously described<sup>37</sup>. Such changes were not observed in non-mutant tissues from PolG<sup>mut</sup> animals such as the liver, or in that of other lipids in the PolG<sup>mut</sup> liver and plasma (Supplementary Fig. 7C). There was also substantial differences in several other lipids in the TA of PolG<sup>mut</sup> mice, particularly in methyl-lipids and cholesterol containing species. Interestingly, when we investigated the abundance of specific CL species in the PolG<sup>mut</sup> TAs, we noted that the majority of CLs that were significantly increased

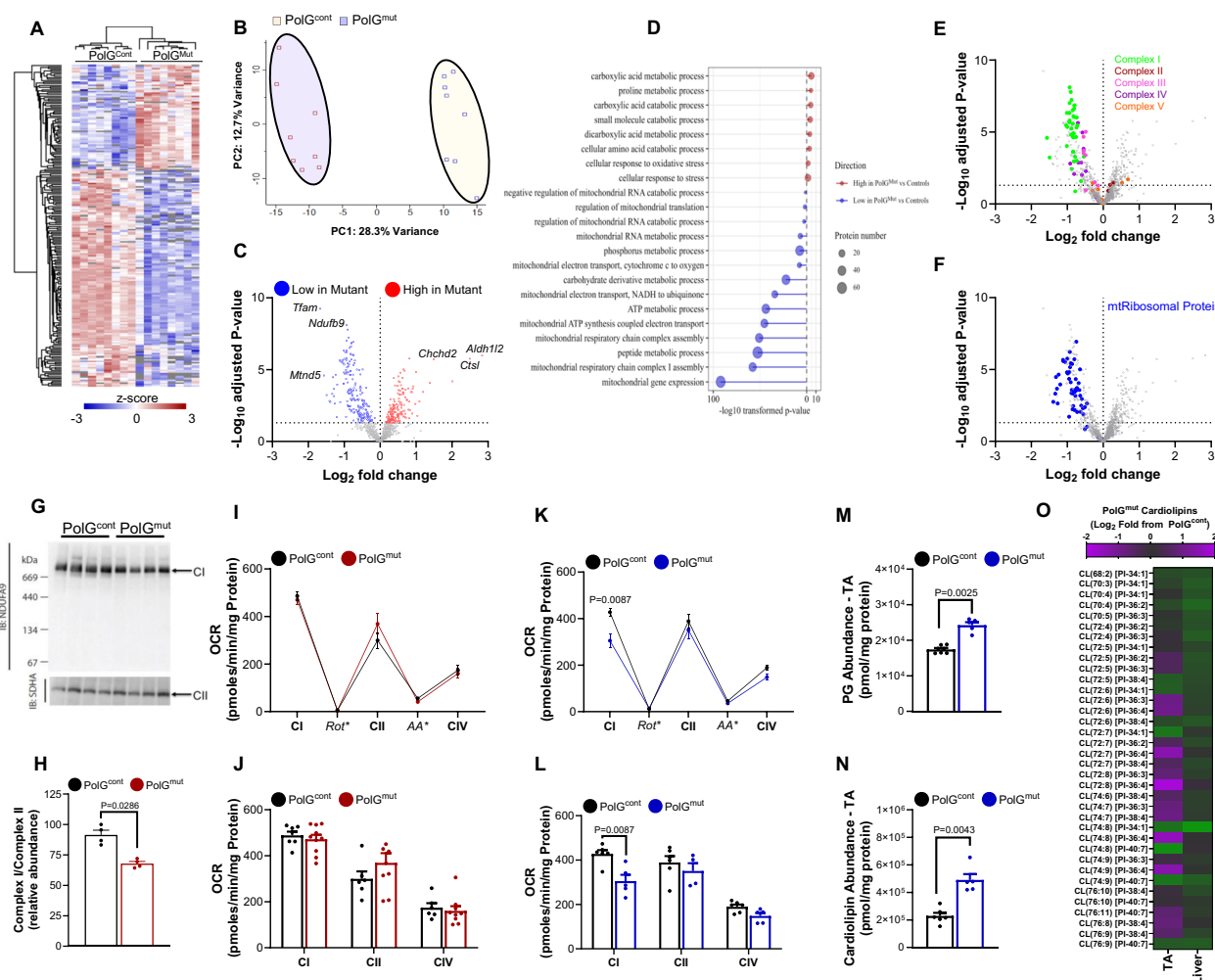


**Fig. 2 | Molecular and functional specific changes in mitochondria induced by muscle specific loss of PolG exonuclease activity.** Protein abundance in mitochondria from skeletal muscle of PolG<sup>cont</sup> and PolG<sup>mut</sup> short term mice was analysed using proteomics. Computational analysis of the data was performed including (A) hierarchical clustering, (B) principal component analysis (PCA) and, (C) volcano plot depicting proteins that were significantly altered, (low=blue dots and high=red dots) in PolG<sup>mut</sup> mitochondria compared to PolG<sup>cont</sup> (grey dots=not significantly altered). D Enrichment analysis of proteins significantly regulated in mitochondria between the genotypes, depicting upregulated pathways in red, and down-regulated pathways in blue. Size of the circle indicates the number of proteins that contribute to the cluster. E Volcano plot of differentially regulated proteins between the genotypes, with the individual proteins of the Electron Transport Chain (ETC Complex I-V) highlighted (CI = green, CII = Red, CII = pink, CIV = purple, CV = orange) and (F) Volcano plot highlighting proteins from the mitochondrial ribosome complex (blue dots). Analyses of proteomic data (A–F) were corrected using Benjamini-Hochberg FDR,  $n = 8$ /group. Isolated mitochondria were also

analysed for functional differences including (G) Blue Native PAGE gel with immunoblot for Complex I (NDUFA9) and Complex II (SDHA) formation and, (H) quantitation of BN-PAGE blots,  $n = 4$ /group. The Seahorse analyser was used on fresh mitochondria isolated from muscle to measure Oxygen Consumption Rate (OCR) for activity of Complex I (CI), Complex II (CII) and Complex IV (CIV) from (I, J) short-term cohort (PolG<sup>cont</sup>  $n = 6$ , PolG<sup>mut</sup>  $n = 9$ ), and (K, L) long-term cohort (PolG<sup>cont</sup>  $n = 6$ , PolG<sup>mut</sup>  $n = 5$ ). Lipidomics was performed in TAs of PolG<sup>cont</sup> and PolG<sup>mut</sup> from long-term cohorts demonstrating the (M) abundance of the cardiolipin pre-cursor lipid phosphatidylglycerol (PG), and (N) total cardiolipin (CL). PolG<sup>cont</sup>  $n = 6$ , PolG<sup>mut</sup>  $n = 5$ . I–N are presented as mean  $\pm$  SEM, with  $P$ -value between control and mutant biological replicates determined by two-sided, unpaired two-tailed t-test (H) or Mann-Whitney test (I–N). O Abundance of individual CL species (fold change from PolG<sup>cont</sup>) in TA and Liver from PolG<sup>cont</sup> and PolG<sup>mut</sup> long-term mice (purple = increased, green = decreased in PolG<sup>mut</sup>), PolG<sup>cont</sup>  $n = 6$ , PolG<sup>mut</sup>  $n = 5$ . Source data for these figures are provided in the Source Data file.

were those which contained at least one phosphatidic acid (PA) as 36:4, which likely represents a PA with two 18:2 containing acyl chain (suggestive of newly synthesised or unmodified CLs) (Fig. 2O), which were also some of the most abundant (Supplementary Fig. 7D). Indeed, some CLs were also reduced in PolG<sup>mut</sup> TA muscles, which were mostly CLs containing a 34:1 PA. These trends were not observed in the liver of PolG<sup>mut</sup> mice where PolG function would be expected to be normal. What the relevance of this CL remodelling is to the phenotype remains unknown, but may reflect the alteration in activity of specific mitochondrial enzymes that are no longer able to modify CLs, or that there is increased generation of new CLs to compensate for disrupted or damaged cristae, consistent with what has been recently postulated in mitochondrialopathies in mice<sup>1</sup>.

Overall, these molecular and functional data indicate a striking molecular change in the mitochondria of muscle from PolG<sup>mut</sup> mice. Whilst consistent with what might be expected from a defect that intrinsically impacts mtDNA integrity, the ensuing alterations in body weight remained unexplained.

### Transcriptional response to deletions in mtDNA in muscle of PolG<sup>mut</sup> Mice

With proteomic, functional and phenotypic readouts indicating an intrinsic defect in mitochondrial activity in PolG<sup>mut</sup> mice, we were interested to understand how these impairments impacted globally on the muscle transcriptional response. To achieve this, we performed bulk RNA-sequencing on TA muscles from the short-term cohort of

PolG<sup>mut</sup> mice, so as to identify those pathways preceding, and perhaps driving intrinsic and systemic effects.

Sequencing analysis was performed on  $n = 6$  of both PolG<sup>cont</sup> and PolG<sup>mut</sup> TA muscles. Hierarchical clustering of differentially regulated genes demonstrated consistent differences amongst samples of each genotype, and that genotypes clustered within their representative groups at the highest level (Fig. 3A). PCA was able to statistically separate the genotypes robustly based on these components (Fig. 3B). Analysis of specific genes that were significantly differentially regulated ( $q < 0.05$ ) identified 492 genes that were downregulated, and 676 genes upregulated in PolG<sup>mut</sup> muscle compared with controls (Fig. 3C and Supplementary Data 3). The most highly significantly regulated genes revealed key players in pathways involved in aminoacyl-tRNA activity, autophagy, the integrated stress response (ISR) and one-carbon metabolism (1C-Met). Further analysis of the principal components revealed some granularity regarding pathways that were contributing to these components, demonstrating a strong influence from pathways including RNA processing, ribosome biogenesis and translation (PC1) (Fig. 3D). Other components suggested contributions from the ETC and oxidative phosphorylation (PC3), and pathways important in cellular remodelling and adhesion (PC5). Pathway enrichment analysis of differentially expressed genes demonstrated significant enrichment in upregulated pathways consistent with those observed in mitochondrial proteomics, which were namely related to alternative energy metabolism and the response to cellular stress and 1C-Met (Fig. 3E), with downregulated pathways associated with extracellular matrix reorganisation and pathways associated with injury repair (Fig. 3F). Moreover, consistent with the observation that mutant mice were losing muscle mass, there was an enrichment for genes related to “neurodegeneration”, “Huntington Disease” and “Mitophagy”, all of which would be an indication that autophagy was being activated. Indeed, when we specifically investigated genes known to be associated with autophagy, we found that *Map1lc3b*, *Ulk2* and *Sqstm1* were all significantly upregulated in mutant muscle (Supplementary Fig. 8A). In support of this, western blots for LC3 in our mutant muscles showed an increased conversion of LC3-I to LC3-II (Supplementary Figs. 8B and C), however this occurred in the absence of any change in total ubiquitination (Supplementary Figs. 8D and E). Overall, these data provide evidence that autophagy was upregulated in mutant muscle and likely explained the loss in muscle mass, prior to that which led to degeneration.

A strong signature that emerged from the RNA-seq data was activation of the integrated stress response (ISR), with several of these genes being altered in the top 20 most differentially expressed genes (Supplementary Fig. 9A). A key initiating process in the activation of the ISR is phosphorylation of eIF2 $\alpha$  at Ser51<sup>38,39</sup>. Accordingly, when we performed Western blotting in a subset of short and long-term muscles from PolG<sup>cont</sup> and PolG<sup>mut</sup> mice for eIF2 $\alpha$  phosphorylation, we demonstrated robust activation of this pathway, particularly in the short term muscles (Supplementary Figs. 9B–D). The ensuing transcriptional response downstream of eIF2 $\alpha$  phosphorylation is well characterised, and we outline the primary canonical members of this pathway in Supplementary Fig. 10A. When we analysed our RNA-seq data for specific changes in these genes, we observed a significant alteration in the expression of ~90% of the ~35 genes involved (Supplementary Fig. 10B). Of note in this list, were two upregulated genes that encode for the peptide hormones FGF21 and GDF15, which are often released due to mitochondrial stress and subsequent ISR activation<sup>40–43</sup>. These proteins are of particular interest in our study because of their recently described impacts on systemic metabolism and weight loss, and indeed these proteins are currently being investigated as biomarkers for mitochondrial myopathies in humans<sup>42,43</sup>, and as potential treatments for metabolic dysregulation<sup>44–48</sup>.

## Systemic consequences of muscle specific activation of the integrated stress response

With RNA-seq data demonstrating an ~180-fold and 25-fold increase in *Fgf21* and *Gdf15* respectively in PolG<sup>mut</sup> muscle, we wanted to confirm the altered expression of these genes using qPCR. Consistently, we observed equivalent fold change in both *Fgf21* and *Gdf15* using qPCR as that measured by RNA-seq in the short-term cohort (Fig. 3G). In older mutant mice, *Fgf21* expression was reduced by about 50% (to ~80-fold) compared to young mice, whilst *Gdf15* expression continued to increase in aged mice to > 200-fold above PolG<sup>cont</sup> mice (Fig. 3H). We further demonstrated that this increased gene expression translated into increased plasma levels, where FGF21 was ~2-fold higher in PolG<sup>mut</sup> mice from the short-term cohort, whilst GDF15 was increased by several hundred fold (Fig. 3I). In mice from the long-term cohort, we noted that FGF21 abundance in the plasma had reduced back to control levels in aged PolG<sup>mut</sup> mice (Fig. 3J), whereas plasma levels of GDF15 were still significantly elevated (~3.5 Fold) compared to PolG<sup>cont</sup> mice. Such levels in the blood of these mice would very likely explain the alterations in fat mass and body weight, as has been shown from data in many prior studies. We hypothesise that chronic activation of these pathways over many weeks, would result in a slight but continuous alteration to whole body metabolism that would eventually result in major reductions in body fat mass.

## Upstream pathways leading to ISR activation in PolG<sup>mut</sup> muscle

Our data provide strong evidence that PolG mutation in muscle leads to chronic activation of the ISR, potentially driving pathogenic phenotypes, but it is not clear from our current data or the literature how this occurs. To decipher what leads to activation of the ISR in our model, we investigated several pathways of interest. Firstly, we did not observe any major alterations in classic “energy sensing” pathways in the muscle of mutant mice, including the Akt, AMP-kinase and mTOR pathways (Supplementary Fig. 11A and B), which is in contrast to what has been observed previously in the global Deletor (TWNK-KO) mouse<sup>40</sup>. Given this outcome, we chose to focus on known activators of the ISR and eIF2 $\alpha$ . We had already demonstrated that phosphorylation of eIF2 $\alpha$  was increased in vivo in mouse PolG<sup>mut</sup> muscle (Supplementary Fig. 9B), and therefore we presumed that one of the four upstream kinases of eIF2 $\alpha$  must also be activated. The four known kinases of eIF2 $\alpha$  are PKR, PERK, HRI and GCN2<sup>49</sup>. The two main kinases implicated in mitochondrial stress are GCN2<sup>50</sup> and HRI<sup>51,52</sup> and therefore, we focussed on GCN2 and HRI pathways in our mutant mice.

Western blots for phosphorylated GCN2 from skeletal muscle of both young and aged mice demonstrated no difference between PolG<sup>cont</sup> and PolG<sup>mut</sup> mice (Supplementary Figs. 11C and D), suggesting that GCN2 is not the upstream pathway to ISR in our model. With regards to the HRI pathway, which has been described to function<sup>53,54</sup> in both an iron dependent<sup>55</sup> and independent<sup>56,57</sup> manner. Mechanistically, this is achieved via activation of the inner mitochondrial membrane protease OMA1, which cleaves the protein DELE1 in mitochondria, allowing cleaved DELE1 (sDELE1) to translocate from mitochondria to the cytosol where it binds and activates HRI<sup>56–58</sup>. Interestingly, breaks in mtDNA have also recently been shown to activate the HRI/DELE1 pathway<sup>51</sup>. We show that in muscle from our mutant model, the abundance of HRI is increased (in aged mice) (Supplementary Figs. 11E and F), whilst the shorter activated variant of the inner mitochondrial membrane protease OMA1, was also increased in our mutant model – again suggesting a disturbance to this pathway (Supplementary Figs. 11E and F) and collectively implicating this pathway in the activation of the ISR in our model.



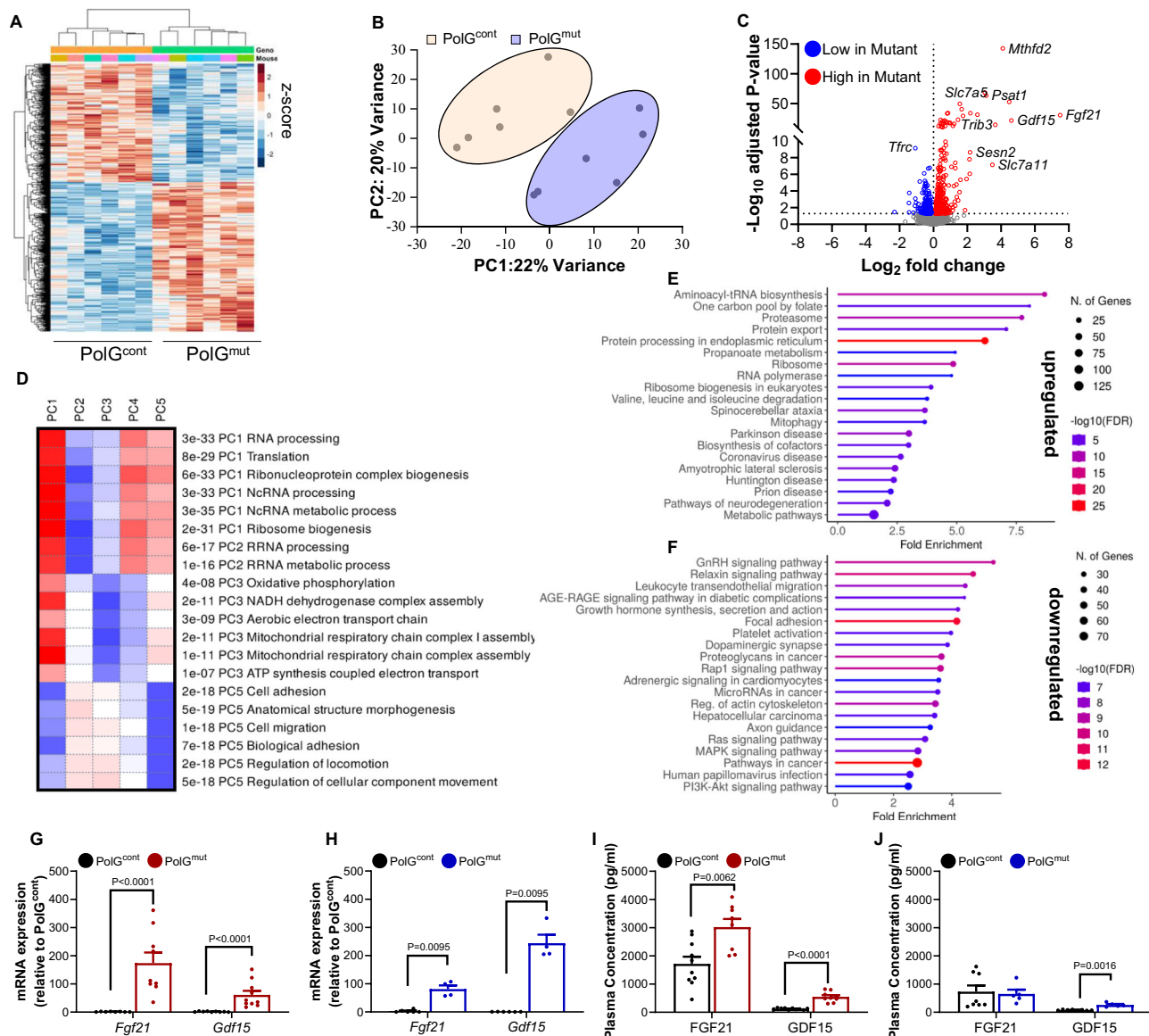


**Fig. 3 | Transcriptional regulation and activation of the ISR in response to muscle specific loss of PolG exonuclease activity.** Unbiased assessment of RNA abundance was analysed from skeletal muscle of PolG<sup>cont</sup> and PolG<sup>mut</sup> short-term mice using bulk RNA-sequencing. Computational analysis of the data was performed including (A) hierarchical clustering of differentially expressed genes, (B) principal component analysis (PCA) between PolG<sup>cont</sup> and PolG<sup>mut</sup> and, (C) volcano plot depicting genes that were upregulated (red dots) and downregulated (blue dots) in PolG<sup>mut</sup> muscle compared to PolG<sup>cont</sup>—grey dots indicate non-significantly altered genes. (D) Specific identification of components driving global changes in principal component analysis. For each pathway, a one-sample t-test on each gene set GOBP was performed, with the adjusted *P*-values used to rank the pathways for each of the first 5 principal components. The pathways are labelled with FDR first, followed by the principal components (duplicated pathways are skipped)

(red=increased, blue=decreased, white=no change). Enrichment analysis (KEGG) on genes demonstrates (E) pathways that were significantly upregulated between the genotypes and (F) pathways that were significantly downregulated between the genotypes. Analyses of transcriptomic data (A–F) were corrected using Benjamini-Hochberg FDR, *n* = 6/group. *Fgf21* and *Gdf15* mRNA expression as determined by qPCR in muscles from (G) short-term (PolG<sup>cont</sup> *n* = 9, PolG<sup>mut</sup> *n* = 10) and (H) long-term (PolG<sup>cont</sup> *n* = 6, PolG<sup>mut</sup> *n* = 4) PolG<sup>cont</sup> and PolG<sup>mut</sup> mice. Gene expression analysis was validated by ELISA for protein abundance of FGF21 and GDF15 in plasma in (I) short-term (PolG<sup>cont</sup> *n* = 10, PolG<sup>mut</sup> *n* = 9) and (J) long-term (PolG<sup>cont</sup> *n* = 5, PolG<sup>mut</sup> *n* = 5) PolG<sup>cont</sup> and PolG<sup>mut</sup> mice. Gene expression and ELISA data are presented as mean ± SEM, with *P*-value between control and mutant biological replicates determined by two-sided, unpaired two-tailed Mann-Whitney test (G–J). Source data for these figures are provided in the Source Data file.

### Altered folate cycle activity underpins the PolG<sup>mut</sup> ISR phenotype

Given the above results, we were intrigued as to what the underlying initiators of the ISR response might be in our mutant model. We reasoned that because many previous triggers of the mtISR have been shown to be metabolites, that alteration in abundance of a particular metabolite in our model may be the trigger. Therefore, we performed a metabolomic screen on the gastrocnemius muscle of PolG<sup>mut</sup> and PolG<sup>cont</sup> mice at both young and aged time points, to identify differentially abundant metabolites in the muscles between genotypes

(Supplementary Data 4). In the short and long term cohorts, we demonstrate that the metabolome is distinct enough to be separated by PCA (Supplementary Figs. 12A and B), but that only a handful of detected metabolites demonstrated a robust and significant (by FDR) change as shown in volcano plots (Supplementary Figs. 12C and D). Enrichment analysis on these data provided more insight, largely confirming our earlier findings which identified major changes in alternative energy pathways (glycolysis, pentose phosphate pathway) and 1C-Met (Fig. 4A, B). To gain further insight into these changes, we next analysed the individual metabolites of these enriched pathways



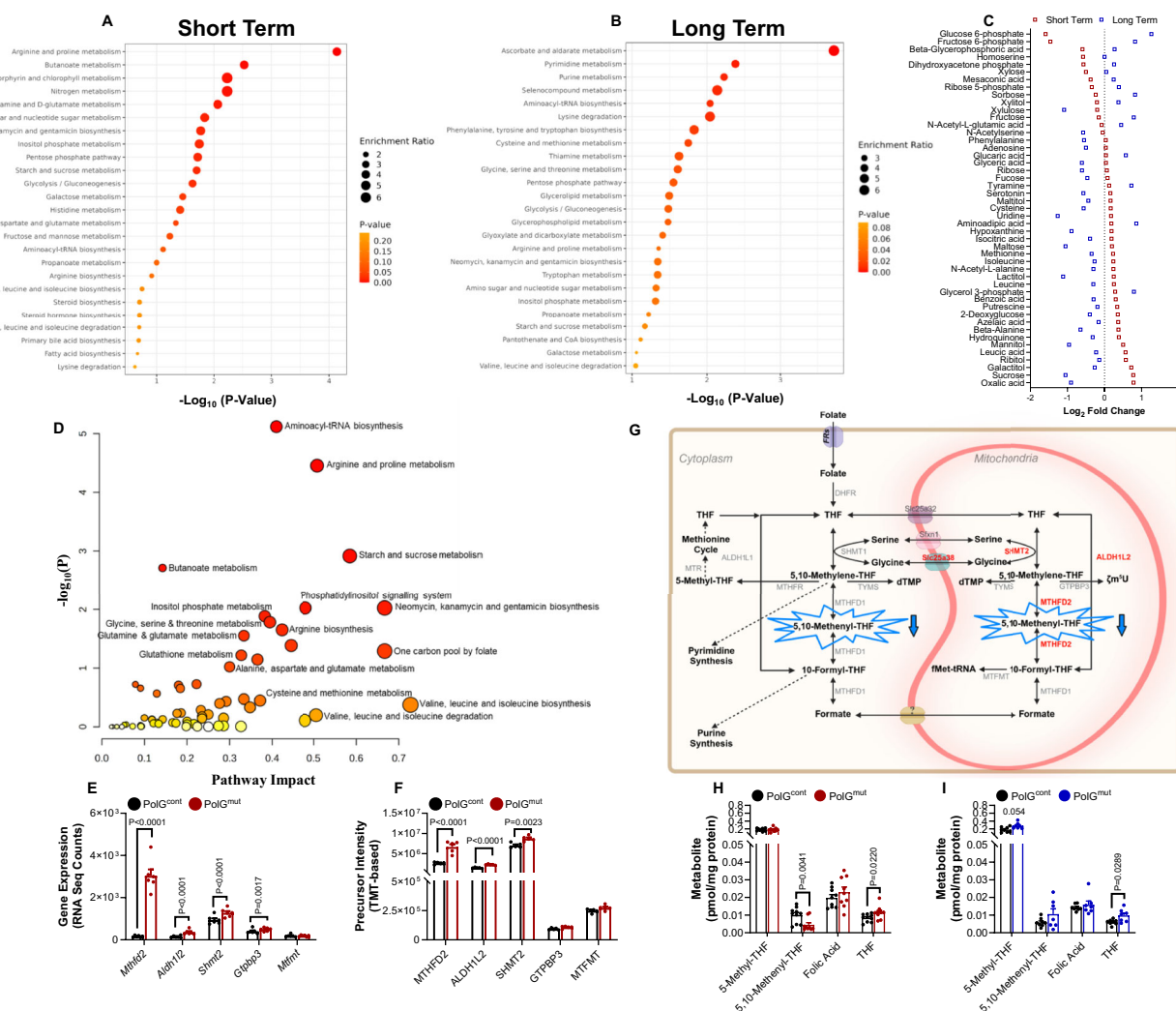


**Fig. 4 | Metabolite alterations in muscle of *PolG*<sup>mut</sup> mice mediated by muscle specific loss of *PolG* exonuclease activity.** Unbiased assessment of metabolite abundance was performed in gastrocnemius muscle of *PolG*<sup>cont</sup> and *PolG*<sup>mut</sup> mice with (A) pathway enrichment analysis (MetaboAnalyst-KEGG) undertaken in short-term and (B) long-term cohorts, where metabolic pathways are listed in order of significance, red gradient indicating *P*-value, and the size of the circle denoting the enrichment ratio. C Metabolites in *PolG*<sup>mut</sup> short term (red) and long term (blue) skeletal muscle that had greater than 0.05-fold change (relative to *PolG*<sup>cont</sup>). D Integrated metabolic pathway analysis (MetaboAnalyst) of short-term skeletal muscle bulk RNA-sequencing and metabolomics data sets, with red gradient indicating *P*-value and circle size indicating pathway impact. Metabolomics data (A–D) was normalised by median and log transformed using MetaboAnalyst 5.0. (short-term: *n* = 8/group & long-term: *PolG*<sup>cont</sup> *n* = 8, *PolG*<sup>mut</sup> *n* = 7). E relevant folate cycle genes detected by RNA-sequencing (*n* = 6/group) and (F) proteins detected by

mitochondrial proteomics, *n* = 5/group. Analyses of transcriptomic data (E) and proteomic data (F) were corrected using Benjamini-Hochberg FDR. G Schematic of the mammalian cytosolic/mitochondrial folate cycle (red text denotes upregulated proteins and blue indicating reduced folate intermediates) in short-term cohort. Targeted metabolomics was performed to determine folate cycle metabolic intermediates in (H) short (*PolG*<sup>cont</sup> *n* = 10, *PolG*<sup>mut</sup> *n* = 9) and (I) long-term (*PolG*<sup>cont</sup> *n* = 8, *PolG*<sup>mut</sup> *n* = 7) cohorts (reduced 5,10-Methenyl-THF highlighted in short term folate cycle schematic in blue). E, F, H, I data are presented as mean ± SEM, with *P*-value between control and mutant biological replicates determined by two-sided, unpaired two-tailed t-test (E, F) or Mann-Whitney test (H, I). THF = Tetrahydrofolate; TMP = Thymidine monophosphate; m5U = 5-taurinomethyluridine. Source data for these figures are provided in the Source Data file. Fig. 4G Created in BioRender. Drew, B. (2025) <https://BioRender.com/t82k138>.

across the two time points (Fig. 4C). These data highlight an interesting reversal of the metabolite profile with time, where for example glycolysis metabolites such as Glucose 6-phosphate and Fructose 6-phosphate were substantially reduced in young *PolG*<sup>mut</sup> mice, but increased in aged mutant mice. Moreover, the pentose phosphate pathway was increased in young mutant animals, but decreased with age. Collectively these data highlight a major rewiring of energy metabolism over time in mutant mice (summarised in Supplementary Fig. 12E).

A further way to investigate this data is to overlay and integrate the various omics outputs. Accordingly, we overlaid the RNA-seq and metabolite data from the short-term cohorts, with specific changes in related enzymes and proteins from these pathways highlighted in

Supplementary Figs. 12F, G. This approach provided significant additional insights that were not previously captured by each method alone (Fig. 4D). Specifically, we identified notable enrichments for butanoate metabolism, glycine/serine metabolism, 1C-Met and folate cycle metabolism. In particular, we identify a major signal in the mutant muscle for enzymes and metabolites that support the synthesis of serine and subsequently intermediates of the mitochondrial folate cycle. Interestingly, serine is a critical co-factor for the enzyme SHMT2, which in the mitochondria catalyses the reversible conversion of serine and tetrahydrofolate (THF) to glycine and 5,10-methenyl-THF – the latter being a precursor to the formation of dUMP, dTMP (purine pathway) and to 10-formyl-THF, which is required for the biosynthesis of formyl-methionine (fMet). fMet is the modified amino acid

responsible for initiating translation of numerous mitochondrial encoded RNAs, and its absence leads to stalling of mitochondrial translation of certain proteins<sup>59</sup>. Furthermore, when revisiting our transcriptomic and proteomic data, we were intrigued to observe that two of the most upregulated genes/proteins in our omics datasets were ALDH1L2 and MTHFD2 (Fig. 4E, F), both of which are critically important in regulating the abundance of 5,10-methenyl-THF. Our findings therefore point to a concerted effort for the mutant cells to increase the levels of THF intermediates, most likely 5,10-methenyl-THF. Such evidence suggests that there is either an insufficient biosynthesis of 5,10-methenyl-THF in mutant muscle, or an increased demand leading to its eventual depletion (Pathway and Summary shown in Fig. 4G).

To investigate this directly, we developed and optimised a mass spectrometry-based assay to quantify the abundance of folate cycle metabolites (Supplementary Data 5). In this analysis we demonstrate that the major folate cycle metabolite reduced in short-term mutant muscle is 5,10-methenyl-THF (Fig. 4H), which appears to mostly be resolved in long term cohorts (Fig. 4I), where we observed a partial resolution of the ISR phenotype, and muscle regeneration. There was no change in other folate cycle metabolites, other than an increase in THF, which is the primary precursor metabolite and thus likely reflects the muscles attempt to continue fluxing substrates through this pathway.

Consistent with this observed deficit in 5,10-methenyl-THF, we identify a specific shuttle of resources towards increased serine synthesis, which likely reflects the cells attempt to increase activity of SHMT2 and thus synthesis of 5,10-methylene-THF. This is demonstrated at both the RNA and protein levels for SHMT2 (Fig. 4E, F). Yet this does not appear to be sufficient to remedy the pathologies present in our mutant muscle. Depleted levels of 5,10-methenyl-THF would also be consistent with a block in mitochondrial protein translation (via flow on effects to 10-formyl-THF and subsequently fMet), which is strongly supported by our data demonstrating reductions in specific mitochondrial proteins, despite an up to 3-fold increase in mitochondrial RNA transcription. Thus, our findings propose that reductions in the abundance of folate cycle intermediates, including 5,10-methenyl-THF, is a contributor to mitochondrial dysfunction in this model, and may be a critical component leading to exacerbation of the ISR and subsequent pathologies in this mutant model.

In summary, we have generated an inducible, tissue-specific PolG exonuclease deficient mouse model, which recapitulates many aspects of previous preclinical models including decrements in PolG activity and mtDNA integrity, and importantly allows tissue specific investigations into key aspects of the condition. This includes an increased rate of mtDNA deletions and promotion of a degenerative phenotype in affected tissues. In this study we induced the PolG mutation in skeletal muscle of 8 week old mice, in which 12 months of homozygous deletion led to a musculo-degenerative phenotype that is preceded by a robust activation of the ISR. The ISR was activated alongside an apparent reduction in abundance of specific folate cycle intermediates, which may be a critical aspect of the subsequent activation of the ISR, and ultimately increased release of the peptide hormones FGF21 and GDF15 into the circulation, the latter leading to systemic alterations in metabolism with resistance to adiposity (Fig. 5).

## Discussion

Herein we confirm and validate the generation of an inducible, tissue-specific mouse model of PolG exonuclease insufficiency, which importantly appears to retain all functions of PolG activity - other than the expected loss of mtDNA proofreading capacity (the specific function regulated by the exonuclease domain). These engineered defects in the PolG enzyme lead to an increase in the abundance of mtDNA deletions and mitochondrial heteroplasmy, which subsequently drives mitochondrial stress responses, perturbations and tissue pathology.

We anticipate that this conditional and temporal PolG mutator mouse model will be a valuable model for the study of one of the most common inherited mitochondriopathies in humans. Moreover, using this unique model in a muscle specific context we have been able to reveal critical new knowledge in pathways associated with activation of the mitochondrial stress response that is relevant to both mouse models of disease and similar conditions in humans – specifically that reduced abundance of specific folate derivatives may be important players in the ensuing activation of the integrated stress response.

In this study we investigated the short (4 month) and long (12 month) term impacts of post-developmental homozygous loss of PolG exonuclease activity specifically in skeletal muscle. It is worth emphasising that this is a post-developmental model, which was induced during adolescence and therefore all phenotypic changes are attributable to responses in mature muscle. Despite the post-developmental nature of this protocol, we still observed faithful recapitulation of key aspects of the global PolG mutator model, namely muscle degeneration and wasting. Whilst the animals demonstrated characteristics of skeletal myopathy, the animals did not display evidence of significant ill health up to one year post-deletion, with an observed mortality of 0% at this time point. This allowed us to study the whole-body impacts of this phenotype in the absence of complicating morbidities including neurodegeneration and heart failure – two common observations in the global mutator models<sup>23,60</sup>. Unexpectedly we also observed a striking reduction in body weight at ~5 months post-mutation, driven at first by a loss of fat mass that with age also resulted in reduced lean mass, which reliably developed in all cohorts studied.

In depth molecular characterisation using proteomics, transcriptomics, lipidomics and metabolomics revealed that mitochondria from these animals had specific reductions in components of the electron transport chain (ETC) and mitochondrial ribosomal machinery. These defects were associated with a robust nuclear activation of stress signalling cascades, which did not include the type 1 interferon response, which has previously been shown to be important in global mutator models<sup>61</sup>, but instead involved the mitochondrial unfolded protein response (mtUPR), integrated stress response (ISR) and alterations in alternative metabolism pathways. These classic hallmarks have been described in other models of “mitochondrial myopathy” and are collectively coined the integrated mitochondrial stress response (mtISR or ISR<sup>mt</sup>)<sup>40</sup>. Whilst the mtISR likely elicited many cellular outcomes, the most prominent in our model was the elevation of muscle derived expression of the peptide hormones FGF21 and GDF15, and their subsequent release into the circulation. Given the large amount of published work and ongoing interest in these peptide hormones, we propose that it is the peripheral response to elevations in plasma FGF21 and GDF15 that likely explains the observed reductions in fat mass in these animals. This being the case however, we were surprised that this model did not demonstrate more striking alterations to metabolic readouts. Given the robust and chronic elevation in plasma FGF21 and GDF15, we expected to observe major differences in glucose/insulin tolerance, and energy expenditure (EE). Many recent papers have demonstrated that exogenous delivery of FGF21 and GDF15 promote substantial metabolic benefit to both rodents and humans via effects on food intake, EE, weight loss and improved glucose tolerance<sup>30,44–46,48</sup>. Indeed, a very recent study also demonstrated that chronic exogenous delivery of GDF15 led to changes in body weight driven not only by reduced food intake, but in concert with a pathway in skeletal muscle that prevents the normal suppression of skeletal muscle energy expenditure<sup>62</sup>. Whilst we observed robust reductions in fat mass and body mass, we were unable to attribute this weight loss to any major detectable differences in food intake or EE. This being said, we did observe a major difference in raw EE, but this was almost completely due to the differences in body weight, and once adjusted via ANCOVA, no significant difference was shown. Therefore,

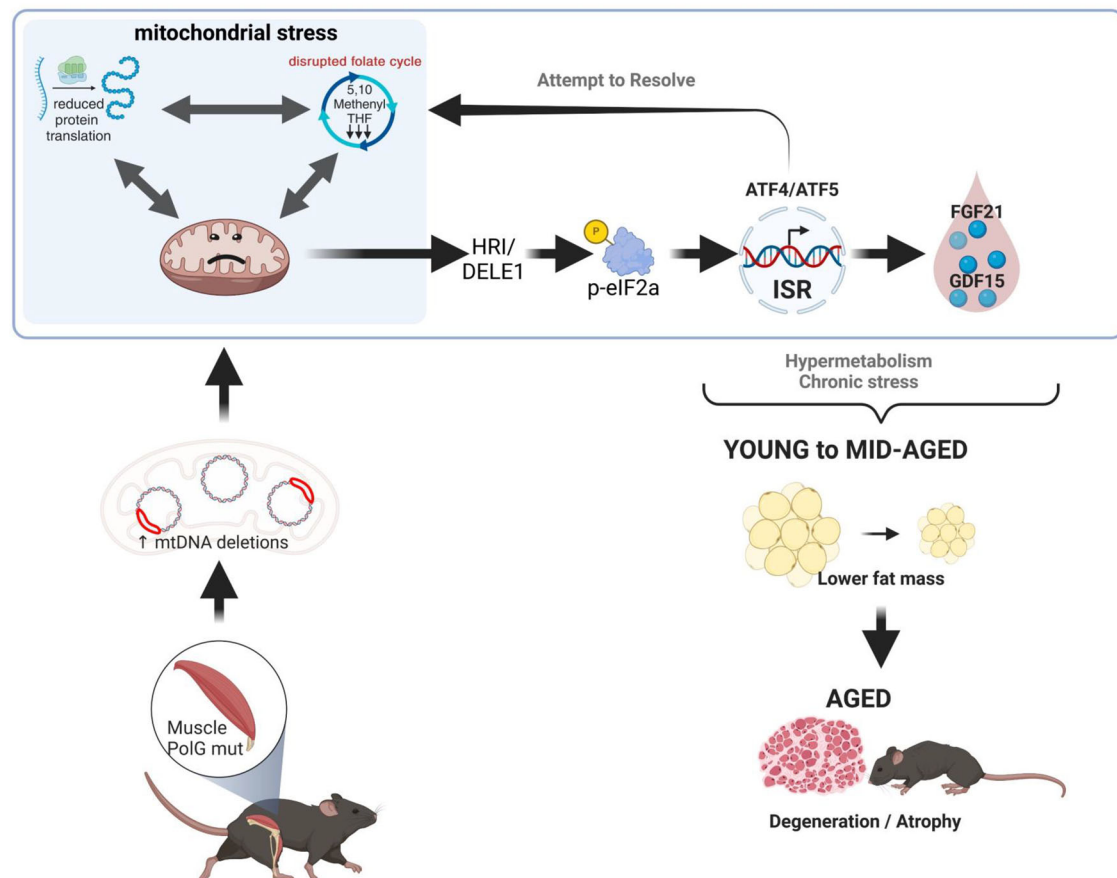


**Fig. 5 | Schematic summarising the tissue-specific and whole body impacts of muscle specific loss of PolG exonuclease activity.** PolG Exonuclease deletion in skeletal muscle leads to an increased mtDNA deletion rate that with age promotes a degenerative phenotype specifically in the mutated tissue (skeletal muscle). This degeneration is preceded by a robust activation of the mitochondrial integrated stress response (ISR), driven in part by reduced protein translation and perturbed

folate cycle activity characterised by a reduced abundance of 5,10-methenyl-THF. The activated ISR leads to an increased release of the peptide hormones FGF21 and GDF15 into the circulation. These series of events alter systemic metabolism that profoundly impact the accretion of fat mass. This figure was Created in BioRender. Drew, B. (2022) BioRender.com/s20n885.

it is likely that small but prolonged changes in food intake and EE are likely responsible for the phenotype observed, which was below the level of detection with the methods we used. Consistent with an improved metabolic status, the glucose excursion curves following GTT were improved in older mice (but not younger mice), when there were much greater reductions in fat mass. This was accompanied by evidence for a likely improvement in insulin sensitivity, as demonstrated by a reduced plasma insulin following a glucose bolus during the GTT in both young and aged mice. In the context of the recent work by Wang et al. demonstrating effects of GDF15 directly on muscle energy expenditure through calcium futile cycling, the body weight effects in our PolG model may relate to increased energy expenditure via this pathway. Whatever the mechanism, these mice in general had only a minor metabolic advantage, which might be useful information when assessing therapeutic options in humans with mitochondrial myopathy. Related to this, given that the mutant mice began to regain weight in the latter stages of the aged experiment, our findings might indicate that chronic elevation of the peptide hormones FGF21 and GDF15, leads to a desensitisation of the periphery to these factors, highlighting important considerations for potential clinical trials planned with these targets.

Consistent with our data, recent literature describing similar intrinsic mitochondrial defects have also shown activation of these stress pathways, particularly in skeletal muscle. This includes models with impaired mitochondrial ribosome machinery<sup>63–65</sup>, mitochondrial protein homeostasis<sup>66</sup>, and mtDNA replication/polymerisation

defects<sup>42,67</sup>. Importantly however, our study demonstrates in a post-developmental PolG related model, robust and chronic increases in the mtISR, with induction of both FGF21 and GDF15 circulating hormones. There have indeed been select examples of increased plasma FGF21 being detected in the global PolG mutator model<sup>68</sup>, however the literature regarding this has been inconsistent. Nevertheless, these findings collectively indicate that elevations in plasma FGF21 and GDF15 may be useful markers for detecting the presence of mitochondrial disease, particularly those which manifest from respiratory chain defects, a proposal that has recently been tested and confirmed in small-scale human studies<sup>43,69</sup>.

Why the ISR pathway and FGF21/GDF15 would be altered in the setting of skeletal muscle mitochondrial dysfunction remains incompletely understood, even though aspects of these pathways have been previously highlighted by several other groups. A teleological explanation for such an outcome is that specific mitochondrial insults elicit a starvation-like response in select tissues<sup>42</sup>, in order to circumvent specific energy deficits. Indeed, FGF21 is increased in the liver in response to starvation<sup>70,71</sup>, which potentially involves nutrient sensing pathways<sup>72</sup>. In muscle, the mTOR pathway has been experimentally implicated in mitochondrial myopathy phenotypes together with activation of the mtISR, where global Twinkle-knock out mice (TWNK-KO/Deletor Mice) demonstrated increased activation of the mTOR pathway in muscle, whilst treatment with the mTOR inhibitor rapamycin, prevented activation of the muscle mtISR and reduced circulating FGF21 levels<sup>40</sup>. Contrary to these findings, we did not observe



activation of the mTOR pathway in our mutator mice, either in the short- or long-term cohorts, suggesting that this is not the mechanism by which the ISR is activated in our model.

Studies continue to investigate the underlying mechanisms relating to activation of the mtISR, with the majority of evidence suggesting that dysfunction in ETC activity is a likely contributor<sup>50,73–75</sup>. Whilst this may be true in some instances, other studies have modelled defects in respiratory chain components in skeletal muscle, and rarely do these studies report weight loss associated with activation of the mtISR<sup>76</sup>. Such observations have also been made in humans, where screening of plasma FGF21 and GDF15 with known mitochondrial disease, demonstrated that FGF21 was almost exclusively elevated in individuals who had mitochondrial translation defects or mtDNA deletions, but not in other patients (including those with Complex I defects)<sup>77</sup>. Thus, it is highly likely that a specific cascade of events must occur in skeletal muscle for the mtISR to be activated, and thus elicit this starvation-like response.

The hypothesis of a specific cascade of events activating the mtISR in skeletal muscle has been postulated and tested previously, particularly through the use of whole-body mouse models of mtDNA deletions (e.g. TWNK-KOs)<sup>42,78</sup>. However as with existing PolG models, such global models cannot avoid complicating morbidities from other central and peripheral tissues, nor rule out defects acquired during development. For example, activation of the mTOR pathway in the Deletor mice (TWNK-KO) may be compensatory to signals received from other tissues, especially as we did not observe a similar activation in our model (where no compensation is likely). A recent study by Mick and colleagues systematically investigated alternative pathways that might lead to activation of the mtISR in cultured myoblasts and myotubes<sup>50</sup>. This study also postulated that there are likely many pathways that can activate the mtISR, which are tissue, cell and context dependent. Ultimately, this group provided evidence for a disruption to amino acid metabolism that was a consistent component to their phenotype, with a specific reduction in asparagine shown to activate the stress kinase GCN2 and subsequently the mtISR. Important insights from this and other studies hint to differential activation of the mtISR in various tissues, even though the same mitochondrial defect may be apparent. This appears to be consistent with work from other groups that implicate HRI, another eIF2 $\alpha$  kinase, playing a role in activating the ISR in response to various stresses on the mitochondria including alterations to iron abundance and breaks in mtDNA. Our findings also suggest that HRI is the likely upstream kinase activating the ISR in our model, whilst also discounting a role for GCN2.

Another notable observation from our studies are the major reduction in mitochondrial ribosomal complexes and other specific protein complexes in the mitochondria, despite a significantly upregulated transcription of mtDNA encoded RNAs. Whilst this is a characteristic observation of mitochondrial stress, the explanations of what drives this phenomena are not as well understood. Specifically, our mitochondrial proteome data demonstrated a substantial depletion of proteins associated with mitochondrial ribosomal function. Conversely, we reveal a major upregulation of all the acyl tRNA synthetase (ARS) enzymes important for protein translation at cytoplasmic ribosomes. This likely highlights a feedback mechanism whereby a loss of protein translation in the mitochondria, subsequently signals for an increased protein translation in the cytoplasm (presumably of proteins that might otherwise be transported into mitochondria), and is a described outcome relating to activation of the ISR. It has been demonstrated previously by others that the ISR activates members of the ATF class of transcription factors, and that ATF5 specifically binds to Amino Acid Starvation Response Elements (AARE) in the nuclear genome following mitochondrial stress, inducing transcription of genes important in one-carbon metabolism including *Mthfd2* and *Psat1*<sup>79</sup>. We also observed elevation in these genes together with the many ARS genes (Supplementary Fig. 10) consistent with an

activation of the amino acid starvation response. Nevertheless, this increase in cytoplasmic translation activity was apparently unable to alleviate the defect, providing evidence that there was a potential deficiency in protein transport across the mitochondrial membrane, as has been proposed previously by others<sup>80</sup>.

The loss of mitochondrial protein translation, and increase in one-carbon and amino acid related genes, fuelled our interests in understanding the underlying triggers for activation of the ISR. As mentioned above, whilst GCN2 and HRI have both been implicated in leading to activation of eIF2 $\alpha$  following mitochondrial stress, the precise molecular triggers of this response are not clear. Our metabolomics analysis of the PolG mutant mice identified notable alterations in serine/glycine metabolism alongside major rewiring of pathways regulating the folate cycle. Work from others have also identified dysregulation of Serine metabolism as being an important component of cellular health particularly relating to mitochondrial dysfunction<sup>81,82</sup>. Our integrative data sets encompassing transcriptome, proteome and metabolome identify a highly coordinated cellular response to promote the synthesis of folate derivatives, notably 5,10-methenyl-THF, and our direct measurement of this metabolite confirms a significant reduction in its abundance, suggesting that pathogenic reductions in this compound are highly likely to be involved in driving, or at least contributing to, the pathological phenotypes in this model. Reductions in 5,10-methenyl-THF are consistent with the underlying defects in mitochondrial protein translation, and subsequent activation of the ISR. The reasons for why there is a deficiency in this metabolite in our model is not currently determinable from the current data, but proposes the exciting possibility that interventions which replenish 5,10-methenyl-THF, might have therapeutic utility in the setting of various mitochondrial disorders.

In conclusion, our novel muscle specific PolG exonuclease mutant model provides several important insights into disease pathology driven by disruptions to mitochondrial integrity and the ISR in skeletal muscle. Notably, this was studied in the absence of complicating pathologies from other affected tissues, allowing for a longer term and more precise understanding of PolG function in skeletal muscle. Moving forward, our conditional model will provide the field with a novel opportunity to investigate mtDNA deletion-driven pathology in almost any tissue of interest, thus significantly advancing our knowledge of disease that is driven by such defects. These opportunities may lead to the identification of novel targets and biomarkers, as well as therapeutics that replenish 5,10-methenyl-THF, with potential relevance to the human condition.

## Limitations

This is the first detailed experimental analysis of this novel PolG mutant mouse model and therefore it is not yet understood how these findings may relate to specific human conditions involving mitochondrial dysfunction. This being said, the clear and chronic activation of the ISR response in this model, together with the robust alterations in folate metabolites, makes this an ideal model to study the specifics of human disease in which ISR and folate pathways are involved. An obvious limitation is that mtDNA genomes were not sequenced in this study, where the nature of stochastic or specific repeated mutations/deletions could be attributed to human conditions. All experiments were conducted with muscle tissues containing mixed fibres, but given there was only a limited amount of specific muscle tissues from each animal cohort, such as tibialis anterior (TA), experimental analysis was performed across different muscle types. However, the same muscle type was used for all experiments that were compared between groups and different animal cohorts (e.g. all metabolomics data performed in gastrocnemius muscles). Limitations exist for metabolomics, transcriptomics and lipidomics analysis where low abundance biomolecules (i.e. some folate metabolites) may have fallen below

the sensitivity threshold of the mass spectrometer, and subsequently, may not have been detected. The use of male mice in the study also restricts our ability to draw conclusions about how female mice may respond to the PolG mutation, mtDNA deletions, and activation of the mtISR.

## Methods

### Animals

All animal experiments were approved by the Alfred Research Alliance (ARA) Animal Ethics committee (E/2030/2012/B), and performed in accordance with the ethical guidelines set out by the National Health and Medical Research Council (NHMRC) of Australia and to those outlined in the ARRIVE guidelines. Floxed PolG mutator mice (PolG<sup>fl/fl</sup>) were generated in-house in collaboration with the Monash Genome Modification Platform using CRISPR to insert LoxP sites within the intron between exons 3&4, and exons 5&6 of the *Polg1* gene (Fig. 1A). Recombination was achieved using the Cre-Lox system by crossing the PolG<sup>fl/fl</sup> mice with ACTA1-CreERT2 mice (C57BL/6J background, Jackson Laboratories, #025750) to generate PolG<sup>fl/fl</sup>;ACTA1-CreERT2<sup>-/-</sup> (PolG<sup>fl/fl</sup>) and PolG<sup>fl/fl</sup>;ACTA1-CreERT2<sup>+/-</sup> (PolG<sup>fl/fl</sup>;Cre) animals. Male mice were bred and genotyped, before being randomly allocated into two separate groups each, totalling four groups altogether. Mice were aged to 6–8 weeks before one group of each genotype received oral gavage of Tamoxifen (80 mg/kg) in sunflower oil for three consecutive days, whilst the other received sunflower oil alone. This resulted in four different groups: PolG<sup>fl/fl</sup>;OIL, PolG<sup>fl/fl</sup>;Cre+OIL, PolG<sup>fl/fl</sup>;TAM (PolG<sup>cont</sup>), PolG<sup>fl/fl</sup>;Cre+TAM (PolG<sup>mut</sup>). Mice were housed at 22 °C on a 12 h light/dark cycle with access to food (chow: SF00-100 Specialty feeds, Australia) and water ad libitum with cages changed weekly. Several separate cohorts of PolG<sup>mut</sup> mice were generated, which were either aged to 5 months (short-term) or to 12 months (long-term) post tamoxifen treatment, together with their respective controls. At the end of the studies, mice were fasted for 4–6 h and then anesthetized with a lethal dose of ketamine/xylazine before blood and tissues were collected, weighed and frozen for subsequent analysis. Some analyses were performed from different muscle depots (i.e. gastrocnemius and tibialis anterior) due to limitations in the amount of tissue, however all muscles were mixed fibre type to reduce variations in phenotypic responses.

### Glucose tolerance test (GTT)

An oral glucose tolerance test (oGTT) was performed at 46 weeks post-tamoxifen in the long-term cohort and at 2, 6, 10 & 18 weeks post-tamoxifen in the short-term cohort, as previously described<sup>83,84</sup>. Briefly, after a 5 h fast mice were administered a bolus of glucose (25% glucose solution) via oral gavage, at a dose of 2 g/kg calculated to lean mass as determined by EchoMRI. Blood glucose was measured at baseline before mice were gavaged, then subsequent measures of blood glucose were analysed at 15, 30, 45, 60, 90 & 120 min post-gavage using a glucometer (Accu Check Performa, Roche Diabetes Care). An insulin ELISA was conducted in conjunction with oGTT in the long-term cohort at 46 weeks post-tamoxifen and in the short-term cohort at 18 weeks post-tamoxifen. Plasma insulin quantification was determined using Mouse Ultra-sensitive Insulin ELISA kit (ALPCO, USA) performed according to the manufacturer's instructions using 5 µl of plasma from 0 and 15 minute time points<sup>85</sup>.

### EchoMRI

Body composition analysis, including lean mass (LM) and fat mass (FM), was analysed in living mice using the 4-in-1 NMR Body Composition Analyzer for Live Small Animals (EchoMRI LLC, Houston, TX, USA). Analysis was performed at designated periods throughout the study according to the recommendations of the manufacturer as previously described<sup>84–86</sup>.

### Whole body energetics

Mice were placed in the Promethion High-Definition Behavioural Phenotyping System for Mice (Sable Systems International, North Las Vegas, NV, USA) at 34 weeks post-tamoxifen for long-term cohorts and at 8 weeks post-tamoxifen for short-term cohorts, for 3 consecutive days as previously described<sup>87</sup>. Recordings for food intake, movement and respirometry, including energy expenditure (EE) and respiratory exchange ratio (RER), were collected over the final 24-h period following an initial acclimation period of 24 hours.

### Gait analysis (DigiGait)

Gait analysis was performed using the DigiGait™ Treadmill System (Mouse Specifics Inc., USA) to assess different aspects of gait, posture, and motor function. DigiGait provides precise quantitative data measurements of gait parameters for each limb independently (left and right forelimbs and hindlimbs). Before each test mice were allowed to acclimatise in the Perspex chamber for 2 min. Digital images of animal paw placement from the ventral plane were then recorded through a clear treadmill that was running at a constant speed of 15 cm/s. Each mouse ran on the treadmill for ~2 minutes to ensure that a consistent 3–4 second period of uniform walking was recorded. For each mouse, videos were analysed using the DigiGait™ Imaging and Analysis software v 12.2 (Mouse Specifics Inc., USA). Measurements were determined for each four limbs independently and reported as either separate limb values or combined and reported as forelimb and hindlimb values.

### Mitochondrial (mt)DNA to nuclear (n)DNA ratio

Mitochondrial content was determined by qPCR using a ratio of mtDNA to nDNA, as previously described<sup>87</sup>. Briefly, tibialis anterior muscle was homogenised in digestion buffer (100 mM NaCl, 10 mM Tris-HCl, 25 mM EDTA, 0.5% SDS, pH 8.0) and then incubated in Proteinase K (250 U/mL) for 1 h at 55 °C. Following this, total DNA was isolated using the phenol-chloroform extraction method. A qPCR reaction was then performed on 2 ng of total DNA using a primer set that amplifies the mitochondrial gene *Mtco3*, and the nuclear gene *Sdha* (see Table 1 for primer sequences). Estimated abundance of each gene was used to generate a ratio of mitochondrial to nuclear DNA (mtDNA/nDNA), and this ratio was compared between genotypes.

### Hang wire strength test

For latency-to-fall hangwire test, mice hung freely from their forepaws without the help of their hind legs or tail, on a wire suspended horizontally between two vertical beams 45 cm above a padded surface. Initially, mice underwent two days of training where mice were repeatedly placed on the wire for a total of 3 minutes per mouse. On day 3, mouse hangtime is recorded. Briefly, one test is completed when the animal lets go and drops onto the padded surface, which is repeated 3 times with a minimum 5 minute break between each test. The amount of time they were able to hang (latency-to-fall) was recorded and averaged over the three tests.

### Skeletal muscle transcriptomics

Bulk RNA sequencing was performed as previously described<sup>85</sup>, and raw data is deposited at ArrayExpress/Annotare. RNA was extracted from tibialis anterior (TA) muscles from each group using The Direct-zol RNA MiniPrep kit according to manufacturer's instructions (Zymo Research). RNA quality for sequencing was determined using the high-sensitivity Agilent RNA ScreenTape Assay for 4200 Tape Station System (Agilent Technologies). Only samples with an RNA Integrity Number (RIN) score > 8 were selected for subsequent analysis. DNA libraries were generated as per the manufacturer's protocol using the NEBNext® Poly(A) mRNA Magnetic Isolation

**Table 1 | Primer sequences**

Gene name	Primer sequence	
	Forward (5' – 3')	Reverse (3' – 5')
<i>mPolG pre-exon3</i>	CGGCTGGTGGAAGAGCGTTA	TTCTGCCCATCCTGCTTGG
<i>mPolG exon4-5</i>	CCAATGGTCCAGCGATCTCA	CTCCCGAGGCTCCTTCTCTA
<i>mPolG post-exon3</i>	CTTTGGCTGGATGACTCTGC	CCCATAGATGCGGCCATAGT
<i>mtDNA TaqI-634</i>	ACTCAAAGGACTTGGCGGTA	AGCCCATTTCTTCCCATTTT
<i>mtDNA Control</i>	CCTATCACCCCTTGCCATCAT	GAGGCTGTGCTTGTGTGAC
<i>mtDNA deletion</i>	ACCCTATTACTGGCTTCAATC	GGGAACGTATGGGCGATAAC
<i>mMyoG</i>	CAACCAGGAGGAGCGCGATCTCCG	AGGCGCTGTGGGAGTTGCATTCAT
<i>mMyoD</i>	GCTGTAATCCATCATGCCATCA	AGGCCGTGGCAGCGA
<i>mActa1</i>	CCAGCCTTCCTTTATCGGTATG	CGGTCAGCGATACCAGGG
<i>mCkm</i>	TGAGGTCTGGGTACTCCTCC	CCTCCACAGCACAGACAGAC
<i>mPax3</i>	ATCGGAGCCTTCATCTGACT	GGCGGATCTAGAAAGGAAGG
<i>mPax7</i>	CGGGTTCTGATTCCACATCT	CGACGAGGAAGGAGACAAGA
<i>mMyh3</i>	CAGAGTGAAAGTCGGGAATG	GAGTGACCATCCACAAGAAC
<i>mMyh8</i>	GATCAGGAGCAGGAATGATG	CCTGTGTGTTCTGTAGTTC
<i>mTnn2</i>	GGGACATCAGCGTTAAAGAG	GCACCATCATGACCAAGAA
<i>mTnni1</i>	GTAGGAGACTGGAGGAAGAA	GACCAAGCATGACACAGA
<i>mTnni2</i>	GATCTCAGGATGGGAGATGAG	CTCCTTCTCAGATTCTCGGC
<i>mMtc3 (mtDNA)</i>	GCAGGATTCTTCTGAGCGTTCT	GTCAGCAGCCTCCTAGATCATGT
<i>mSdha (nucDNA)</i>	TGGACCATCTTCTATGC	TACTACAGCCCCAAGTCT
<i>mFgf21</i>	TACACAGATGACGACCAAGA	GGCTTCAGACTGGTACACAT
<i>mGdf15</i>	GACTTGGGCTGGAGCGACTG	GCAGGCGTGCTTTGATCTGC

*m* mouse.

Module kit (New England Biolabs). 1 µg total RNA per sample was inputted and adaptor ligation and PCR enrichment was performed using the NEBNext® Multiplex Oligos for Illumina® kit as per manufacturer's instructions. Libraries for each of the 12 samples were individually bar coded using n6-barcodes and library quantity and quality were assessed as per manufacturer's instructions using the Agilent D1000 ScreenTape Assay for 4200 TapeStation System. DNA libraries were pooled and then ran on a NovaSeq 6000 sequencer at the Centre of Genomic Medicine at the Alfred Hospital/Monash University. Reads were performed as paired-end with an average read length of 66 base pairs with a total of > 400 M reads collectively across all 12 samples, equating to ~30 million reads or more per sample.

### Transcriptomics analysis and gene set enrichment

RNA-sequencing data were processed and analysed similarly to that demonstrated previously<sup>85</sup>. Briefly, quality of raw sequence reads were assessed by FastQC. Based on the quality reports, read trimming was not required (Phred score > 35). Optical duplicates were removed using BBMap clumpify (<https://github.com/BioInfoTools/BBMap>) BBMap version 38.75. The processed reads were aligned to mm10 version of the mouse genome using STAR aligner. Mapped genes were counted using Feature Counts and lowly expressed genes were determined as those that had <1 count per million (CPM) in at least 8 samples, and subsequently removed. Trimmed Mean of M-values normalization (TMM) was performed to account for library size variation between samples. PCA was conducted with TMM normalised Log<sub>2</sub> values to confirm separation of samples based on group, with no significant RNA concentration or read depth effect. Differential expression analysis was performed using DESeq2, ShinyGO.77, and iDEP.951<sup>88</sup>. Gene Set Enrichment Analysis of upregulated and down-regulated gene sets was performed using ShinyGO.77 with Kyoto Encyclopedia of Genes and Genomes (KEGG) and Gene Ontology databases<sup>89</sup>.

### Lipidomics

Lipidomics was analysed in plasma, TA muscle, and liver PBS homogenates as described previously in detail<sup>90</sup>. Briefly, lipids were extracted from tissues/plasma using a 1:1 Butanol/Methanol extraction method, before application to ESI-MS/MS analysis<sup>90</sup>. Quantification of lipids from MS analysis was performed using Mass Hunter Software (Agilent). Cardiolipins were annotated as their sum composition and the composition of the assigned product ion measured.

### Skeletal muscle metabolomics

Gas Chromatography Mass Spectrometry (GC-MS) polar metabolomic analysis was performed in skeletal muscle (gastrocnemius) from young and aged mice ( $n=8$ /condition except long term PolG<sup>mut</sup>,  $n=7$ ). Tissues were cryomilled in 600 µL of 3:1 methanol/water (containing 2 nmol of <sup>13</sup>C<sub>5</sub><sup>15</sup>N valine and <sup>13</sup>C<sub>6</sub> sorbitol as internal standards), using a Bertin Technologies Precellys bead mill coupled to a Cryolys cooling unit. The lysates were incubated at 4 °C for 10 min with continuous agitation followed by centrifugation at 4 °C for 10 min at 16000 g, and supernatant transferred to fresh tubes. A 35 µL aliquot of each sample was pooled to create the pooled biological quality control (PBQC). 35 µL of each sample and the PBQC were transferred into HPLC inserts and evaporated at 30 °C to complete dryness in preparation for GC-MS analysis. Dried samples were derivatized online using the Shimadzu AOC6000 autosampler robot. Derivatisation was achieved by the addition of 25 µL methoxyamine hydrochloride (30 mg/mL in pyridine) followed by shaking at 37 °C for 2 h. Samples were then derivatised with 25 µL of N,O-bis (trimethylsilyl)trifluoroacetamide with trimethylchlorosilane (BSTFA with 1% TMCS) for 1 h at 37 °C. The sample was allowed to equilibrate at room temperature for 1 h before 1 µL was injected onto the GC column using a hot needle technique. The GC-MS system used comprised of an AOC6000 autosampler, a 2030 Shimadzu gas chromatograph and a TQ8050NX triple quadrupole mass spectrometer (Shimadzu, Japan), with an electron ionization source (-70eV). ~603 targets were collected using the Shimadzu Smart



Metabolite Database, where each target comprised a quantifier MRM along with a qualifier MRM, which covers ~381 endogenous metabolites and multiple stable isotopically labelled internal standards. Resultant data was processed using Shimadzu LabSolutions Insight software, where peak integrations were visually validated and manually corrected where required. Enrichment and integration with transcriptomic data was performed using MetaboAnalyst 5.0 with Kyoto Encyclopedia of Genes and Genomes (KEGG).

### Analysis of folate intermediates by mass spectrometry

Liquid Chromatography Mass Spectrometry (LC-MS) analysis of folate intermediates was performed in skeletal muscle (gastrocnemius) from short and long-term mice cohorts (short term  $n=9$ –10, long term  $n=7$ –8). The folate extraction method was based on previous publications<sup>91,92</sup>, with some modifications. Extraction buffer was prepared with LC-MS grade water (Merck, Germany), containing 50 mM HEPES, 5 mM of ascorbic acid, 5 mM citric acid (Merck, Germany), and 10 mM of EDTA (Merck, Germany). The pH was adjusted to pH 7 using 1 M solution of sodium hydroxide (Merck, Germany). 15–40 mg of skeletal muscle was homogenised in 400  $\mu$ L of the extraction buffer, plus 2.2  $\mu$ M of 13C-d3-levomefolate, using a TissueLyserII (Qiagen, USA) for 40 s, and sonicated with a Misonix S-4000 Sonicator (Thermo Fisher, USA) for 20 s at amplitude 25. The samples were centrifuged at 6000 rpm at 10 °C for 20 min and the supernatant was purified by solid-phase extraction using 30 mg Oasis HLB reverse phase cartridges (Waters, USA) with a 24-port Visiprep vacuum manifold (Merck, Germany). The cartridges were conditioned with 2 mL of acetonitrile and methanol, and then equilibrated with 2 mL of extraction buffer. The supernatant was loaded onto the cartridge, and subsequently washed with 3 mL of extraction buffer. The samples were then eluted with elution buffer, consisting of 7 parts water plus 1% formic acid, and 1 part 1:1 acetonitrile/methanol (pH 5). Eluted samples were transferred to glass vials with inserts and stored at –80 °C.

**Liquid chromatography mass spectrometry (LC-MS/MS).** The LC-MS/MS method was based on an application note from Thermo Scientific<sup>93</sup> with adjustments. The detection of folate metabolites was performed on an Agilent 6495 C QqQ mass spectrometer coupled with an Agilent 1290 Infinity III HPLC system on a Poroschell 120 Aq-C18 column (2.1  $\times$  150 mm, 2.7  $\mu$ m, Agilent), with thermostat set to 30 °C. Mass spectrometry analysis was performed in positive ion mode with dynamic schedule multiple reaction monitoring (transitions are presented in Supplementary Fig. 13C). The following mass spectrometer conditions were used: gas temperature 200 °C, gas flow rate 18 L/min, nebulizer 45 psi, sheath gas temperature 400 °C, capillary voltage 2500 V, and sheath gas flow 12 L/min. The running solvent consisted of solvent A: 100% water containing 0.5% acetic acid, and solvent B: 80% acetonitrile/20% methanol (v/v). 5  $\mu$ L of sample was injected with a flow rate of 0.5 mL/min. The sample analytical gradient was as follows: starting at 10% B for 1 min, increasing to 50% B at 4 min, then to 95% B to 4.1 min, hold at 95% B to 4.5 min, then decreasing to 10% to 4.6 min, and finally hold at 10% B to 6 min (total run time of 6 minutes). Relative concentrations were calculated by normalising the analyte peak areas to the internal standard. Standard stock solution of the 13C-d3-labelled internal standard, levomefolate (Cayman Chemicals, USA), was prepared as 1 mg/mL in 3:1 water/methanol, containing 5 mM of ascorbic acid (Merck, Germany) and 5 mM citric acid (Merck, Germany).

### Quantitative PCR (qPCR)

RNA was isolated from tissues using RNeasy reagent and isopropanol precipitation. cDNA was generated from RNA using MMLV reverse transcriptase (Invitrogen) according to the manufacturer's instructions. qPCR was performed on 10 ng of cDNA using the SYBR-green method on a QuantStudio 7 Flex Real-Time PCR System, using primer

sets outlined in Table 1. Primers were designed to span exon-exon junctions where possible, and were tested for specificity using BLAST (Basic Local Alignment Search Tool; National Centre for Biotechnology Information). Amplification of a single amplicon was estimated from melt curve analysis, ensuring an expected temperature dissociation profile was observed. Quantification of a given gene was determined by the relative mRNA level compared with control using the delta-CT method, which was calculated after normalisation to one of two housekeeping genes; *Ppia* or *Rplp0*.

### Mitochondrial isolation

For isolation of mitochondria, quadriceps muscles were incubated and minced in ice-cold isolation buffer A (220 mM Mannitol, 70 mM Sucrose, 20 mM HEPES, 2 mM Tris-HCl, 1 mM EDTA/EGTA, pH 7.2) + 0.4% (w/v) fatty acid free BSA and then homogenized with a glass dounce homogenizer. The homogenate was centrifuged at 650 g for 5 min at 4 °C and the pellet was discarded, and the supernatant transferred to a fresh tube. The supernatant was repeatedly centrifuged at 650 g for 5 minutes until very little material was pelleted. The supernatant was then transferred to a high-speed centrifuge tube and centrifuged at 10,000 g for 5 minutes and the supernatant was discarded, and the crude mitochondrial pellet resuspended in isolation buffer A. Mitochondria were re-pelleted by centrifuging at 10,000 g for 5 minutes, and the supernatant was discarded, and the pellet resuspended in 1 ml of isolation buffer B (220 mM Mannitol, 70 mM Sucrose, 10 mM Tris-HCl, 1 mM EDTA, pH 7.2). The final pellet was collected by centrifuging at 10,000 g for 5 minutes, discarding the supernatant and resuspending the pellet in either 1 $\times$  PBS for proteomic analysis or isolation buffer B.

### Random Mutation Capture Assay (RMCA) and Droplet Digital PCR (ddPCR)

The RMCA was performed similarly to that previously described<sup>24</sup>. Briefly, mitochondria were isolated from skeletal muscle as described above. Total DNA was then extracted using the phenol chloroform precipitation method. 50 ng of mtDNA was digested for 6 hours with *TaqI* enzyme, with fresh enzyme added every hour before a final overnight incubation followed by inactivation at 80 °C. 5 ng of digested mtDNA was directly analysed on a BioRad QX200 Droplet Digital PCR System using primers that span the *TaqI* sensitive 634 site, where as 0.05 ng of digested mtDNA was used for detection of the control, *TaqI* insensitive site (mtCont) (see Table 1 for primer sequences). Assays were performed using EvaGreen reaction mix according to the manufacturer's instructions using the following conditions: dissociation (95 °C for 30 s), annealing (61.8 °C for 1 min) and extension (72 °C for 1.5 min) for 50 cycles. Only samples where >10,000 droplets were quantified and included in subsequent analysis.

### Conventional PCR for mtDNA Deletions

To visualise mtDNA deletions we performed conventional PCR on isolated mtDNA from skeletal muscle, and resolved the amplicons on 0.8% agarose gels. Briefly, 10 ng of mtDNA precipitated from skeletal muscle mitochondria (previously treated with DNase I), was amplified using Phusion Polymerase according to the manufacturer's instructions, using the "mtDNA deletion" primers outlined in Table 1 (which flank the major arc of the mtDNA molecule; ~10 kb). The following conditions were used in the amplification reaction: dissociation (95 °C for 30 s), annealing (60 °C for 30 sec) and extension (72 °C for 5 min) for 40 cycles.

### SDS-PAGE and immunoblot

Gastrocnemius muscles were lysed in radio-immunoprecipitation assay (RIPA) buffer supplemented with protease and phosphatase inhibitors. Matched protein quantities were separated by SDS-PAGE and transferred to PVDF membranes. Membranes were blocked in 3% skim milk for 2 h and then incubated with primary antibody (see

**Table 2 | Antibodies for western blot**

Antibody	raised in	size (kDa)	Company	Cat #
Pan 14-3-3	Mouse	30	Santa Cruz	sc1657
Anti-Mouse HRP	Goat	-	Bio-Rad	1706516
Anti-Rabbit HRP	Goat	-	Bio-Rad	1706515
Phospho GCN2 Thr899	Rabbit	220	CST	94668
Total GCN2	Rabbit	220	CST	3302
Phospho mTOR Ser2448	Rabbit	289	CST	5536
Phospho AMPK Thr172	Rabbit	63	CST	2535
Phospho Akt Ser473	Rabbit	60	CST	4060
Phospho eIF2a Ser51	Rabbit	37	CST	3597
Total eIF2a	Rabbit	37	CST	9722
Pan Akt1/2	Rabbit	60	CST	4691
NDUFA9	Rabbit	39	In-house (Monash)	-
EIF2AK1 (HRI)	Rabbit	71	MyBioSource	MBS2538144
OMA1	Mouse	40/60	Santa Cruz	sc-515788
SDHA	Mouse	71	Abcam	ab14715
LC3A/B	Rabbit	14/16	CST	12741
Ubiquitin	Rabbit	-	CST	58395
Total AMPK	Rabbit	62	CST	5831

CST Cell Signaling Technologies.

Table 2 for details) overnight at 4 °C. After incubation with primary antibodies, membranes were washed and probed with their respective HRP-conjugate secondary anti-mouse or anti-rabbit (BioRad) antibodies in 3% skim milk for 2 h at room temperature, then visualised with enhanced chemiluminescent substrate (Pierce). Approximated molecular weights of proteins were determined from a co-resolved molecular weight standard (BioRad, #1610374). Image Lab Software (BioRad) was used to perform densitometry analyses, and all quantification results were normalized to their respective loading control or total protein.

### Blue Native-PAGE

Mitochondria from skeletal muscle were isolated by differential centrifugation as previously described<sup>36</sup>. Protein concentrations were determined by bicinchoninic acid assay (BCA; Thermo Fisher Scientific). Mitochondria were aliquoted and frozen at -80 °C until required. Blue Native (BN)-PAGE was performed as described previously<sup>36</sup>. Briefly, mitochondria were solubilized in detergent buffer (20 mM Bis-Tris pH 7.0, 50 mM NaCl, 10% (w/v) glycerol) containing 1% digitonin for 10 minutes on ice, followed by centrifugation at 16,000 g for 10 minutes. The clarified supernatant containing mitochondrial complexes was then added to one-tenth of the volume of 10x BN-PAGE loading dye (5% (w/v) Coomassie blue G250, 500 mM ε-amino n-caproic acid, 100 mM Bis-Tris pH 7.0) before loading onto the gel. Following electrophoresis, transfer onto PVDF membrane (Merck; IPVH00010) was performed using an Invitrogen Power Blotter System (Thermo Fisher) according to manufacturer's instructions and membranes were incubated with primary and secondary antibodies (See Table 2 for details). Bands were visualised with Clarity Western ECL chemiluminescent substrate (BioRad; 1705061) on a BioRad ChemiDoc XRS+ imaging system according to the manufacturer's instructions. Densitometry was performed as described previously<sup>94</sup>. Pixel intensity was measured in the BioRad software Image Lab (version 5.2.1) by

taking the intensity of a region of interest. Background signal was subtracted by taking a region of the same size away from the region of interest. Signal intensities were then normalized to the intensity of the loading control and taken as a percentage of the highest sample intensity. Densitometry data was then analysed in GraphPad Prism (version 9.3.1).

### Plasma FGF21 & GDF15

Commercial ELISA kits for FGF21 (R&D Systems, #MF2100) and GDF15 (R&D Systems, #MGD150) were used to measure respective plasma concentration as per manufacturer's instructions.

### Isolated mitochondrial respiration

Oxygen consumption rates were measured in isolated mitochondria from the quadriceps muscle of mice, as previously described<sup>95</sup>. To examine mitochondrial function and respiration, oxygen consumption in isolated mitochondrial preps was measured using an XFe96 Seahorse Bioanalyzer (Agilent, USA). Protein was quantified in fresh isolated mitochondrial preps from quadriceps muscle of mice using BCA (Pierce Reagent kit). A total of 3 µg of isolated mitochondria in 180 µl Mitochondrial Assay Solution (MAS) buffer (Sucrose 70 mM, Mannitol 220 mM, KH<sub>2</sub>PO<sub>4</sub> 5 mM, MgCl<sub>2</sub> 5 mM, HEPES 2 mM, EGTA 1 mM, BSA fatty acid free 0.2 %, pH 7.4 adjusted with KOH 1 mol/L) was loaded into a 96 well seahorse cell culture plate (Seahorse XFe96 FluxPak) and centrifuged at 2000 g for 15 min to adhere the mitochondria to the bottom of the plate. To examine sequential electron flow through different complexes of the electron transport chain, an electron flow assay was performed. The electron flow assay was used to determine Complex I, Complex II and Complex IV mediated respiration with sequential injections of Rotenone 2 µM, Succinate 10 mM, Antimycin-A 4 µM, and L-ascorbate 10 mM + N,N,N',N'-Tetramethyl-P-Phenylene-diamine (TMPD) 100 µM. For the electron flow assay, isolated mitochondria were adhered to 96 well plate in MAS media supplemented with Sodium Pyruvate 10 mM, Malate 10 mM and FCCP 4 µM.

### Proteomics

Label free and tandem mass tag (TMT)<sup>96</sup> nano liquid-chromatography/mass spectrometry (nLC/MS) proteomics was performed as previously described<sup>96,97</sup> with some modifications.

### Sample homogenisation, protein reduction, alkylation and diges-

**tion.** Semi-pure mitochondrial extracts were quantified by Bradford Protein Assay and 15 µg of protein for each sample was reduced (10 mM dithiothreitol, DTT) for 1 hr at 25 °C and alkylated (20 mM iodoacetamide) for 30 minutes at 25 °C in the dark, before binding of protein to magnetic beads as previously described<sup>98</sup>. Magnetic bead slurry was prepared by mixing SpeedBeads™ magnetic carboxylate modified particles (Cytiva, 65152105050250, 45152105050250) at 1:1 (v:v) ratio, washing with MS-grade water and reconstituted to a final concentration of 100 µg/µL. The beads were added to the samples at 10:1 beads-to-protein ratio and ethanol added to a final concentration of 50% (v/v). Protein-bound magnetic beads were washed three times with 200 µL of 80% ethanol and reconstituted in 50 µL of 50 mM triethylammonium bicarbonat (TEAB) pH 8.0. Protein digestion was performed with Lysyl Endopeptidase (enzyme:substrate 1:100, 125-05061, Wako Pure Chemical Industries) and trypsin (enzyme:substrate 1:50, Promega V5113) overnight at 37 °C with agitation (1,000 rpm). Peptide digests were collected from the supernatant, dried by vacuum centrifugation and stored at -80 °C. For label-free strategy (*n*=8 per group), peptides were reconstituted in 0.07% trifluoroacetic acid and quantified by Fluorometric Peptide Assay (Thermo Fisher Scientific, 23290).

**TMT peptide labelling and high-pH fractionation.** For TMT-based labelling, anhydrous peptide digests were reconstituted in 50 mM

TEAB pH 8.5 and quantified by fluorometric peptide assay (23290, Thermo Fisher Scientific). Peptides were labelled with 11-plex TMT according to the manufacturer's instructions with minor modifications (Thermo Fisher Scientific, A34808, lot UG287488/278919). In brief, each 11-plex experiment contained 10 different chemical tags for peptide labelling (i.e., groups labelled  $n=5$ ; WT-MUT-WT-MUT-WT-MUT-WT-MUT-WT-MUT). The eleventh tag was used for generating reference channel made by a pooled peptide digest from all samples. A list of the sample labelling strategy is available in PRIDE proteomeXchange (PXD033029). Normalised peptide samples (15  $\mu$ g) were labelled with 11 plex-TMT (A34808, Thermo Fisher Scientific) at 4:1 label-to-peptide ratio for 2 hr and quenched with 0.5% (v/v) hyoxylamine for 30 min at RT. Labelled peptide samples were acidified with 3% (v/v) formic acid (FA) and pooled into a new microtube. Pooled samples were further desalted using Sep-Pak tC18 96-well  $\mu$ Elution (186002318, Waters). Desalted peptide elutions were lyophilised by vacuum-based speedVac for 1 hr and reconstituted in 25 mM ammonium formate, pH 10 for high pH reversed phase (RP) microscale fractionation. In-house X-RPS Stagetips were used for peptide binding and peptides eluted using acetonitrile (2–50%, v/v) in 25 mM ammonium formate, pH 10. A total of 16 fractions were pooled into 3 samples using alternating combinations and lyophilised by speedVac. Peptide samples were reconstituted in 0.07% trifluoroacetic acid (TFA) and quantified using Colormetric peptide assay (23275, Thermo Fisher Scientific).

#### NanoLC and mass spectrometry

**For label-free proteomics.** Spectra acquired in data dependent acquisition on an Q Exactive HF-X benchtop Orbitrap mass spectrometer coupled to an UltiMate™ NCS-3500RS nano-HPLC (Thermo Fisher Scientific) as previously described<sup>29</sup>. Peptides (360 ng) were loaded (Acclaim PepMap100 C18 3  $\mu$ m beads with 100 Å pore-size, Thermo Fisher Scientific) and separated (1.9  $\mu$ m particle size C18, 0.075  $\times$  200 mm, Nikkoy Technos Co. Ltd) with a gradient of 2–28% acetonitrile containing 0.1% formic acid over 95 mins followed by 28–80% from 95–98 mins at 300 nL min<sup>-1</sup> at 55 °C (butterfly portfolio heater, Phoenix S&T). An MS1 scan was acquired from 350–1,650 m/z (60,000 resolution,  $3 \times 10^6$  automatic gain control (AGC), 128 msec injection time) followed by MS/MS data-dependent acquisition (top 25) with collision-induced dissociation and detection in the ion trap (30,000 resolution,  $1 \times 10^5$  AGC, 60 msec injection time, 28% normalized collision energy, 1.3 m/z quadrupole isolation width). Unassigned precursor ions charge states and slightly charged species were rejected and peptide match disabled. Selected sequenced ions were dynamically excluded for 30 sec. Data was acquired using Xcalibur software v4.5 (Thermo Fisher Scientific). For spectral library generation and high-pH fractionation, anhydrous peptide digests from mutant and WT/control (pooled) were individually reconstituted in 25 mM ammonium formate, pH 10 for high pH reversed phase (RP) microscale fractionation. In-house X-RPS Stagetips were used for peptide binding and peptides eluted using acetonitrile (2–50%, v/v) in 25 mM ammonium formate, pH 10. A total of 8 fractions were lyophilised by speedVac. Peptide samples were reconstituted in 0.07% trifluoroacetic acid (TFA) analysed in single shot proteomics as described<sup>99</sup>.

**For TMT-based proteomics.** TMT-labelled peptides were analysed on a Dionex 3500RS nanoUHPLC coupled to an Orbitrap Eclipse Tribrid mass spectrometer equipped with nanospray ion source in positive, data-dependent acquisition mode. Peptides were separated using an Acclaim Pepmap RSLC analytical column (Dionex-C18, 100 Å, 75  $\mu$ m  $\times$  50 cm) with an Acclaim Pepmap nano-trap column (Dionex-C18, 100 Å, 75  $\mu$ m  $\times$  2 cm), and a gradient of 3–80% (0–3 min, acetonitrile containing acetonitrile and 0.1% (v/v) formic acid over 240 min at 300 nL min<sup>-1</sup> at 50 °C. Peptides were injected into the enrichment column at

an isocratic flow of 5  $\mu$ L/min of 2% (v/v) acetonitrile containing 0.1% (v/v) formic acid for 6 min, applied before the enrichment column was switched in-line with the analytical column. An MS1 scan was acquired from 375–1,500 m/z (120,000 resolution, isolation window of 0.7 Thomson) in 'top speed' acquisition mode with 3 s cycle time on the 3 most intense precursor ions; ions with charge states of 2 to 7 were selected. AGC target was set to standard with auto maximum injection mode, followed by MS/MS data-dependent acquisition with high-field collision-induced dissociation and detection in the ion trap ( $5 \times 10^4$  AGC, 70-ms injection time, normalized collision energy of 38, 0.7 m/z quadrupole isolation width). Activation time of 35 ms and activation Q of 10. Analysis of fragment ions was carried out in the ion trap using the 'Turbo' speed scanning mode. Dynamic exclusion was activated for 30 s, with data was acquired using Xcalibur software. The mass spectrometry proteomics raw files and data analysis files have been deposited to the ProteomeXchange Consortium (<http://proteomecentral.proteomexchange.org>) via the PRIDE partner repository with identifier (label-free/library: PXD039029; TMT-label: PXD033029).

**Proteomics: data processing and bioinformatics.** MS raw files were analysed using MaxQuant (v1.6.14) software<sup>100</sup> and peptide lists were searched against musculus protein database (SwissProt (TaxID=10090) (55,470; Jan 2021) including contaminants database with the Andromeda search engine. For LFQ-based analyses (in combination with spectral library), cysteine carbamidomethylation was selected as a fixed modification and N-terminal acetylation and methionine oxidations as variable modifications. Data was processed using trypsin/P and LysC as the proteolytic enzymes with up to 2 missed cleavage sites allowed. Further processing using match between runs (MBR) and label free quantification (LFQ) algorithm were employed. Peptides were identified with an initial precursor mass deviation of up to 7 ppm and a fragment mass deviation of 20 ppm with a minimum length of 7 amino acids. False discovery rate (FDR) was 0.01 for both the protein and peptide by searching against a reverse database. For TMT-based analyses, reporter ion MS2 (11plex TMT) settings were employed. Additional protein/peptide analysis was performed using Proteome Discoverer (v.2.5, Thermo Fisher Scientific) with the Sequest HT search engine in combination with the Percolator semi-supervised learning algorithm<sup>101</sup>. Fragment match spectral analysis in Proteome Discoverer was used to export sequence specific peptide spectra.

Contaminants, and reverse identification were excluded from further data analysis. High confident protein identification required more than one unique or razor peptides per protein group. Data analysis was performed using the Perseus (v1.6.14.0) package and R programming language<sup>99</sup>. Protein intensities were log2 transformed and normalized using quantile normalization from R package preprocessCore. The histogram of the precursor intensity distribution and the boxplot of correlation covariance were visualized using R package ggplot2. Proteins with no missing values were subjected to downstream visualization and statistical analysis using Perseus of the MaxQuant computational platform<sup>102</sup>. Proteins were subjected to PCA and student's t-test. g:Profiler and Reactome databases were utilized for functional enrichment and network/pathway analysis, significance  $p < 0.05$ . Data demonstrating successful identification of the primary razor peptide from the PolG protein, is shown as the spectral analysis in Supplementary Fig. 13A and the tabled parent ions in Supplementary Fig. 13B.

#### Histology

TA muscles were fixed in formalin and mounted in paraffin before 4  $\mu$ m sections were cut on a Leica microtome. All sections were stained with Hematoxylin & Eosin, and slide images were captured using an



Olympus Slide scanner VS120 (Olympus, Japan) and viewed in the accompanying software (OlyVIA Build 13771, Olympus, Japan). Fibre diameter was assessed on imaged sections using Aperio Imagescope Software (Leica). Analysis was performed on at least 2 sections from each mouse, and at least 5 mice from each group. A minimum of 25 fibres were counted across 5 different fields of view per section. Centralised nuclei were quantified in sectioned images (section area =  $863\ \mu\text{m} \times 550\ \mu\text{m}$ ,  $n = 5\text{--}6/\text{group}$ ) by labelling all nuclei and calculating the percentage of centralised nuclei to total nuclei, with ~150 nuclei counted per image.

### Scanning transmission electron microscopy

Scanning Transmission Electron Microscopy (STEM) was performed in fresh tibialis anterior (TA) muscle samples that were excised from 12 month old PolG<sup>mut</sup> and PolG<sup>cont</sup> mice. Excised TA muscle was cut into 0.5 mm sections and immediately placed into primary fixative (2.5% glutaraldehyde, 2% paraformaldehyde in 0.1 M sodium cacodylate buffer) and stored overnight at 4 °C. The tissues were then rinsed in fresh sodium cacodylate buffer for 3 × 15 min. Secondary fixation was performed using 1% osmium tetroxide and 1.5% potassium ferricyanide in cacodylate buffer for 1 h at room temperature. The tissues were then washed in dH<sub>2</sub>O for 3 × 15 min. Fixed tissues were dehydrated with increasing concentrations of ethanol for 15 min, consisting of 30, 50, 70, 90 and 100% ethanol. The ethanol was removed and replaced with 100% propylene oxide. Dehydrated tissues were incubated in a mixture of Epon resin and propylene oxide at a ratio of 1:1 for 6 h at RT, followed by a 2:1 Epon/propylene oxide mixture overnight. Tissues were incubated in 100% freshly made Epon resin for 6 h, followed by another 100% resin change overnight. The tissues were then placed into Beem capsules in 100% resin and the resin polymerised for 48 h in an oven at 60 °C. Resin embedded tissue was sectioned with a Diatome diamond knife using a Leica UCS ultramicrotome. Sections of thickness 70–90 nm were collected onto 150 mesh copper grids and stained sequentially with 1% uranyl acetate for 10 min and lead citrate for 5 min.

TEM grids with stained sections of muscle were loaded into the Nova NanoSEM 450 using the grid holder stage. An overview image of the loaded grids was captured using the navigation camera (NavCam) and loaded into the Maps 2.1 program. Each grid was assigned a new project name and destination folder for tile scans. The STEM detector was inserted, and live imaging begun at 10 kV and a spot size of 3. A low magnification montage consisting of 10 × 10 tiles was created for each grid in STEM mode to visualize the muscle fibres contained within each TEM section. Large area maps of muscle fibres were created by collecting 20 × 20 (400) individual tiles in X & Y, each taken at a magnification of 2500× with a dwell time of 3 μs and a resolution of 3072 × 2048 pixels. The tiles were stitched together in X & Y using the FIJI (ImageJ) program to create each high-resolution map. Each image file was assigned a blinded file name to remove bias during analysis. The blinded images were then manually assessed for mitochondrial and myofiber abnormalities.

### Statistical analyses

All data were expressed as mean ± standard error of the mean (SEM) unless otherwise stated.

Normality was checked using Shapiro-Wilk normality tests. All statistical analyses in animal studies were analysed by repeated measures two-way ANOVA (for normally distributed data), other than where explicitly detailed. Lipidomics, tissue analysis and cell-based experiments were analysed by ANOVA with post hoc testing (Fishers LSD) where appropriate, or paired Student's t test or Mann-Whitney test unless otherwise stated. Analyses were performed using PRISM9 software and a  $p$  value of  $p < 0.05$  was considered statistically significant.

### Data inclusion and exclusion criteria

For animal experiments, phenotyping data points were excluded using the following pre-determined criteria: if the animal was unwell at the time of analysis, there were technical issues identified (such as failed beam breaks in Promethion), or data points were identified as outliers using Tukey's Outlier Detection Method ( $1.5\ \text{IQR} < Q1$  or  $1.5\ \text{IQR} > Q3$ ). If repeated data points from the same mouse/sample failed QC based on predetermined criteria or several data points were outliers as per Tukey's rule, the entire animal was excluded from that given analysis (i.e., during glucose tolerance tests, indicating inappropriate gavage). For in vivo and in vitro tissue and molecular analyses, data points were only excluded if there was a technical failure (i.e., poor RNA quality such as RIN = < 7, failed amplification in qPCR, failed injection in mass spectrometer) or the value was biologically improbable. This was performed in a blinded fashion (i.e., on grouped datasets before genotypes were known).

### Reporting summary

Further information on research design is available in the Nature Portfolio Reporting Summary linked to this article.

### Data availability

All processed data are available in the included Supplementary Figs. and files, reporting summary or in online repositories as listed below. Source data are also provided with this paper in the "Source Data" file. Raw proteomics data can be found at Proteome Exchange (label-free library: PXD039029; TMT-label: PXD033029). Raw RNA-sequence data have been deposited in the Genome Sequence Archive in National Genomics Data Center, China National Center for Bioinformation / Beijing Institute of Genomics, Chinese Academy of Sciences (<https://ngdc.cncb.ac.cn/gsa> GSA: CRA022003). Raw Metabolomics data is deposited at Figshare.com and accessible through the following link (<https://doi.org/10.6084/m9.figshare.28191746>). Source data are provided with this paper.

### References

- Lee, R. G. et al. Deleterious variants in CRLS1 lead to cardiolipin deficiency and cause an autosomal recessive multi-system mitochondrial disease. *Hum. Mol. Genet.* **31**, 3597–3612 (2022).
- Johns, D. R. Mitochondrial, D. N. A. and disease. *N. Engl. J. Med.* **333**, 638–644 (1995).
- Fontana, G. A. & Gahlon, H. L. Mechanisms of replication and repair in mitochondrial DNA deletion formation. *Nucleic acids Res.* **48**, 11244–11258 (2020).
- Falkenberg, M., Larsson, N. G. & Gustafsson, C. M. DNA replication and transcription in mammalian mitochondria. *Annu. Rev. Biochem.* **76**, 679–699 (2007).
- Anderson, S. et al. Sequence and organization of the human mitochondrial genome. *Nature* **290**, 457–465 (1981).
- Andrews, R. M. et al. Reanalysis and revision of the Cambridge reference sequence for human mitochondrial DNA. *Nat. Genet.* **23**, 147 (1999).
- Rackham, O. & Filipovska, A. Organization and expression of the mammalian mitochondrial genome. *Nat. Rev. Genet.* **23**, 606–623 (2022).
- Copeland, W. C. The mitochondrial DNA polymerase in health and disease. *Sub-Cell. Biochem.* **50**, 211–222 (2010).
- Copeland, W. C. & Longley, M. J. DNA polymerase gamma in mitochondrial DNA replication and repair. *TheScientificWorldJournal* **3**, 34–44 (2003).
- Kaupilla, T. E. S., Kaupilla, J. H. K. & Larsson, N. G. Mammalian mitochondria and aging: an update. *Cell Metab.* **25**, 57–71 (2017).
- Chan, S. S. & Copeland, W. C. DNA polymerase gamma and mitochondrial disease: understanding the consequence of POLG mutations. *Biochimica et. Biophysica acta* **1787**, 312–319 (2009).

12. Kujoth, G. C. et al. Mitochondrial DNA mutations, oxidative stress, and apoptosis in mammalian aging. *Sci. (N. Y., NY)* **309**, 481–484 (2005).
13. Trifunovic, A. et al. Premature ageing in mice expressing defective mitochondrial DNA polymerase. *Nature* **429**, 417–423 (2004).
14. Hiona, A. et al. Mitochondrial DNA mutations induce mitochondrial dysfunction, apoptosis and sarcopenia in skeletal muscle of mitochondrial DNA mutator mice. *PLoS one* **5**, e11468 (2010).
15. Tzoulis, C. et al. Molecular pathogenesis of polymerase  $\gamma$ -related neurodegeneration. *Ann. Neurol.* **76**, 66–81 (2014).
16. Rahman, S. & Copeland, W. C. POLG-related disorders and their neurological manifestations. *Nat. Rev. Neurol.* **15**, 40–52 (2019).
17. Belmonte, F. R. et al. Digital PCR methods improve detection sensitivity and measurement precision of low abundance mtDNA deletions. *Sci. Rep.* **6**, 25186 (2016).
18. Damas, J. et al. Mitochondrial DNA deletions are associated with non-B DNA conformations. *Nucleic acids Res.* **40**, 7606–7621 (2012).
19. Greaves, L. C., Reeve, A. K., Taylor, R. W. & Turnbull, D. M. Mitochondrial, D. N. A. and disease. *J. Pathol.* **226**, 274–286 (2012).
20. Stumpf, J. D. & Copeland, W. C. Mitochondrial, D. N. A. replication and disease: insights from DNA polymerase  $\gamma$  mutations. *Cell. Mol. Life Sci.: CMLS* **68**, 219–233 (2011).
21. Stewart, J. B. & Chinnery, P. F. The dynamics of mitochondrial DNA heteroplasmy: implications for human health and disease. *Nat. Rev. Genet.* **16**, 530–542 (2015).
22. Tynismaa, H. & Suomalainen, A. Mouse models of mitochondrial DNA defects and their relevance for human disease. *EMBO Rep.* **10**, 137–143 (2009).
23. Dai, D. F. et al. Age-dependent cardiomyopathy in mitochondrial mutator mice is attenuated by overexpression of catalase targeted to mitochondria. *Aging Cell* **9**, 536–544 (2010).
24. Vermulst, M., Bielas, J. H. & Loeb, L. A. Quantification of random mutations in the mitochondrial genome. *Methods (San. Diego, Calif.)* **46**, 263–268 (2008).
25. Uoselis, L. et al. Temporal landscape of mitochondrial proteostasis governed by the UPR(mt). *Sci. Adv.* **9**, eadh8228 (2023).
26. Aydin, J. et al. Increased mitochondrial  $\text{Ca}^{2+}$  and decreased sarcoplasmic reticulum  $\text{Ca}^{2+}$  in mitochondrial myopathy. *Hum. Mol. Genet.* **18**, 278–288 (2009).
27. Joseph, A. M. et al. Dysregulation of mitochondrial quality control processes contribute to sarcopenia in a mouse model of premature aging. *PLoS one* **8**, e69327 (2013).
28. Tynismaa, H. et al. Mutant mitochondrial helicase Twinkle causes multiple mtDNA deletions and a late-onset mitochondrial disease in mice. *Proc. Natl Acad. Sci. USA* **102**, 17687–17692 (2005).
29. Claridge, B. et al. Proteome characterisation of extracellular vesicles isolated from heart. *Proteomics* **21**, e2100026 (2021).
30. Rath, S. et al. MitoCarta3.0: an updated mitochondrial proteome now with sub-organelle localization and pathway annotations. *Nucleic acids Res.* **49**, D1541–d1547 (2021).
31. Rudler, D. L. et al. Fidelity of translation initiation is required for coordinated respiratory complex assembly. *Sci. Adv.* **5**, eaay2118 (2019).
32. Mimaki, M., Wang, X., McKenzie, M., Thorburn, D. R. & Ryan, M. T. Understanding mitochondrial complex I assembly in health and disease. *Biochimica et. biophysica acta* **1817**, 851–862 (2012).
33. Lazarou, M., Thorburn, D. R., Ryan, M. T. & McKenzie, M. Assembly of mitochondrial complex I and defects in disease. *Biochimica et. biophysica acta* **1793**, 78–88 (2009).
34. Swalwell, H. et al. Respiratory chain complex I deficiency caused by mitochondrial DNA mutations. *Eur. J. Hum. Genet.: EJHG* **19**, 769–775 (2011).
35. McKenzie, M. & Ryan, M. T. Assembly factors of human mitochondrial complex I and their defects in disease. *IUBMB life* **62**, 497–502 (2010).
36. Formosa, L. E. et al. Dissecting the roles of mitochondrial complex I intermediate assembly complex factors in the biogenesis of complex I. *Cell Rep.* **31**, 107541 (2020).
37. Acoba, M. G., Senoo, N. & Claypool, S. M. Phospholipid ebb and flow makes mitochondria go. *J. Cell Biol.* **219**, e202003131 (2020).
38. Marintchev, A. & Ito, T. eIF2B and the integrated stress response: a structural and mechanistic view. *Biochemistry* **59**, 1299–1308 (2020).
39. Taniuchi, S., Miyake, M., Tsugawa, K., Oyadomari, M. & Oyadomari, S. Integrated stress response of vertebrates is regulated by four eIF2 $\alpha$  kinases. *Sci. Rep.* **6**, 32886 (2016).
40. Khan, N. A. et al. mTORC1 regulates mitochondrial integrated stress response and mitochondrial myopathy progression. *Cell Metab.* **26**, 419–428.e415 (2017).
41. Ribas, F., Villarroja, J., Hondares, E., Giral, M. & Villarroja, F. FGF21 expression and release in muscle cells: involvement of MyoD and regulation by mitochondria-driven signalling. *Biochemical J.* **463**, 191–199 (2014).
42. Tynismaa, H. et al. Mitochondrial myopathy induces a starvation-like response. *Hum. Mol. Genet.* **19**, 3948–3958 (2010).
43. Suomalainen, A. et al. FGF-21 as a biomarker for muscle-manifesting mitochondrial respiratory chain deficiencies: a diagnostic study. *Lancet Neurol.* **10**, 806–818 (2011).
44. Looma, R. et al. Safety, pharmacokinetics, and pharmacodynamics of pegzofermin in patients with non-alcoholic steatohepatitis: a randomised, double-blind, placebo-controlled, phase 1b/2a multiple-ascending-dose study. *lancet Gastroenterol. Hepatol.* **8**, 120–132 (2023).
45. Talukdar, S. et al. A long-acting FGF21 molecule, PF-05231023, decreases body weight and improves lipid profile in non-human primates and type 2 diabetic subjects. *Cell Metab.* **23**, 427–440 (2016).
46. Sanyal, A. et al. Pegbelfermin (BMS-986036), a PEGylated fibroblast growth factor 21 analogue, in patients with non-alcoholic steatohepatitis: a randomised, double-blind, placebo-controlled, phase 2a trial. *Lancet (Lond., Engl.)* **392**, 2705–2717 (2019).
47. Wang, D. et al. GDF15: emerging biology and therapeutic applications for obesity and cardiometabolic disease. *Nat. Rev. Endocrinol.* **17**, 592–607 (2021).
48. Benichou, O. et al. Discovery, development, and clinical proof of mechanism of LY3463251, a long-acting GDF15 receptor agonist. *Cell Metab.* **35**, 274–286.e210 (2023).
49. Pakos-Zebrucka, K. et al. The integrated stress response. *EMBO Rep.* **17**, 1374–1395 (2016).
50. Mick, E. et al. Distinct mitochondrial defects trigger the integrated stress response depending on the metabolic state of the cell. *eLife* **9**, e49178 (2020).
51. Fu, Y. et al. breaks activate an integrated stress response to reestablish homeostasis. *Mol. cell* **83**, 3740–3753.e3749 (2023).
52. Eckl, E. M., Ziegemann, O., Krumwiede, L., Fessler, E. & Jae, L. T. Sensing signaling and surviving mitochondrial stress. *Cell. Mol. Life Sci.: CMLS* **78**, 5925–5951 (2021).
53. Han, A. P. et al. Heme-regulated eIF2 $\alpha$  kinase (HRI) is required for translational regulation and survival of erythroid precursors in iron deficiency. *EMBO J.* **20**, 6909–6918 (2001).
54. Suragani, R. N. et al. Heme-regulated eIF2 $\alpha$  kinase activated Atf4 signaling pathway in oxidative stress and erythropoiesis. *Blood* **119**, 5276–5284 (2012).
55. Sekine, Y. et al. A mitochondrial iron-responsive pathway regulated by DELE1. *Mol. cell* **83**, 2059–2076 (2023).
56. Fessler, E. et al. A pathway coordinated by DELE1 relays mitochondrial stress to the cytosol. *Nature* **579**, 433–437 (2020).
57. Guo, X. et al. Mitochondrial stress is relayed to the cytosol by an OMA1-DELE1-HRI pathway. *Nature* **579**, 427–432 (2020).

58. Yang, J. et al. DELE1 oligomerization promotes integrated stress response activation. *Nat. Struct. Mol. Biol.* **30**, 1295–1302 (2023).
59. Morscher, R. J. et al. Mitochondrial translation requires folate-dependent tRNA methylation. *Nature* **554**, 128–132 (2018).
60. Dai, Y. et al. Behavioral and metabolic characterization of heterozygous and homozygous POLG mutator mice. *Mitochondrion* **13**, 282–291 (2013).
61. Lei, Y. et al. Elevated type I interferon responses potentiate metabolic dysfunction, inflammation, and accelerated aging in mtDNA mutator mice. *Sci. Adv.* **7**, eabe7548 (2021).
62. Wang, D. et al. GDF15 promotes weight loss by enhancing energy expenditure in muscle. *Nature*, **619**, 143–150 (2023).
63. Agnew, T. et al. A wars2 mutant mouse model displays OXPHOS deficiencies and activation of tissue-specific stress response pathways. *Cell Rep.* **25**, 3315–3328.e3316 (2018).
64. Formichi, P. et al. Fibroblast growth factor 21 and grow differentiation factor 15 are sensitive biomarkers of mitochondrial diseases due to mitochondrial transfer-RNA mutations and mitochondrial DNA deletions. *Neurological Sci.: Off. J. Ital. Neurological Soc. Ital. Soc. Clin. Neurophysiol.* **41**, 3653–3662 (2020).
65. Kang, S. G. et al. Differential roles of GDF15 and FGF21 in systemic metabolic adaptation to the mitochondrial integrated stress response. *iScience* **24**, 102181 (2021).
66. Oliveira, A. N. & Hood, D. A. Effect of Tim23 knockdown in vivo on mitochondrial protein import and retrograde signaling to the UPR(mt) in muscle. *Am. J. Physiol. Cell Physiol.* **315**, C516–c526 (2018).
67. Tan, K. et al. Mitochondrial SSBP1 protects cells from proteotoxic stresses by potentiating stress-induced HSF1 transcriptional activity. *Nat. Commun.* **6**, 6580 (2015).
68. Wall, C. E. et al. High-fat diet and FGF21 cooperatively promote aerobic thermogenesis in mtDNA mutator mice. *Proc. Natl Acad. Sci. USA* **112**, 8714–8719 (2015).
69. Sturm, G. et al. OxPhos defects cause hypermetabolism and reduce lifespan in cells and in patients with mitochondrial diseases. *Commun. Biol.* **6**, 22 (2023).
70. Zhang, Y. et al. The starvation hormone, fibroblast growth factor-21, extends lifespan in mice. *eLife* **1**, e00065 (2012).
71. Fazeli, P. K. et al. FGF21 and the late adaptive response to starvation in humans. *J. Clin. Investig.* **125**, 4601–4611 (2015).
72. Ji, K. et al. Skeletal muscle increases FGF21 expression in mitochondrial disorders to compensate for energy metabolic insufficiency by activating the mTOR-YY1-PGC1 $\alpha$  pathway. *Free Radic. Biol. Med.* **84**, 161–170 (2015).
73. McLaughlin, K. L., Kew, K. A., McClung, J. M. & Fisher-Wellman, K. H. Subcellular proteomics combined with bioenergetic phenotyping reveals protein biomarkers of respiratory insufficiency in the setting of proofreading-deficient mitochondrial polymerase. *Sci. Rep.* **10**, 3603 (2020).
74. Liu, S., Liu, S. & Jiang, H. Multifaceted roles of mitochondrial stress responses under ETC dysfunction - repair, destruction and pathogenesis. *FEBS J.* **289**, 6994–7013 (2022).
75. Bao, X. R. et al. Mitochondrial dysfunction remodels one-carbon metabolism in human cells. *eLife* **5**, e10575 (2016).
76. Alam, M. T. et al. Skeletal muscle mitochondria of NDUFS4 $^{-/-}$  mice display normal maximal pyruvate oxidation and ATP production. *Biochimica et. biophysica acta* **1847**, 526–533 (2015).
77. Lehtonen, J. M. et al. FGF21 is a biomarker for mitochondrial translation and mtDNA maintenance disorders. *Neurology* **87**, 2290–2299 (2016).
78. Forsström, S. et al. Fibroblast growth factor 21 drives dynamics of local and systemic stress responses in mitochondrial myopathy with mtDNA deletions. *Cell Metab.* **30**, 1040–1054.e1047 (2019).
79. Nikkanen, J. et al. Mitochondrial DNA replication defects disturb cellular dNTP pools and remodel one-carbon metabolism. *Cell Metab.* **23**, 635–648 (2016).
80. Schäfer, J. A., Bozkurt, S., Michaelis, J. B., Klann, K. & Münch, C. Global mitochondrial protein import proteomics reveal distinct regulation by translation and translocation machinery. *Mol. cell* **82**, 435–446.e437 (2022).
81. Yang, L. et al. Serine catabolism feeds NADH when respiration is impaired. *Cell Metab.* **31**, 809–821 (2020).
82. Handzlik, M. K. & Metallo, C. M. Sources and sinks of serine in nutrition, health, and disease. *Annu Rev. Nutr.* **43**, 123–151 (2023).
83. Bond, S. T., Kim, J., Calkin, A. C. & Drew, B. G. The antioxidant moiety of MitoQ imparts minimal metabolic effects in adipose tissue of high fat fed mice. *Front. Physiol.* **10**, 543 (2019).
84. Bond, S. T. et al. Tissue-specific expression of Cas9 has no impact on whole-body metabolism in four transgenic mouse lines. *Mol. Metab.* **53**, 101292 (2021).
85. Bond, S. T. et al. Deletion of Trim28 in committed adipocytes promotes obesity but preserves glucose tolerance. *Nat. Commun.* **12**, 74 (2021).
86. Lancaster, G. I. & Henstridge, D. C. Body composition and metabolic caging analysis in high fat fed mice. *J.Vis. Exp.* **135**, 57280 (2018).
87. Zhuang, A. et al. SOD2 in skeletal muscle: New insights from an inducible deletion model. *Redox Biol.* **47**, 102135 (2021).
88. Ge, S. X., Son, E. W. & Yao, R. iDEP: an integrated web application for differential expression and pathway analysis of RNA-Seq data. *BMC Bioinforma.* **19**, 534 (2018).
89. Ge, S. X., Jung, D. & Yao, R. ShinyGO: a graphical gene-set enrichment tool for animals and plants. *Bioinformatics* **36**, 2628–2629 (2019).
90. Alshehry, Z. H. et al. An Efficient Single Phase Method for the Extraction of Plasma Lipids. *Metabolites* **5**, 389–403 (2015).
91. Patring, J. D. & Jastrebova, J. A. Application of liquid chromatography-electrospray ionisation mass spectrometry for determination of dietary folates: effects of buffer nature and mobile phase composition on sensitivity and selectivity. *J. Chromatogr. A* **1143**, 72–82 (2007).
92. Liu, J., Pickford, R., Meagher, A. P. & Ward, R. L. Quantitative analysis of tissue folate using ultra high-performance liquid chromatography tandem mass spectrometry. *Anal. Biochem* **411**, 210–217 (2011).
93. Doyle, R. et al. LC-MS-MS quantitative analysis of Folic Acid, its metabolites and derivatives in serum for clinical research use. <https://tools.thermofisher.com/content/sfs/posters/PO-65010-LC-MS-Folates-Serum-ASMS2017-PO65010-EN.pdf> (2017).
94. Formosa, L. E. et al. Mitochondrial COA7 is a heme-binding protein with disulfide reductase activity, which acts in the early stages of complex IV assembly. *Proc. Natl. Acad. Sci. USA* **119**, e211035711 (2022).
95. Watt, K. I. et al. Yap regulates skeletal muscle fatty acid oxidation and adiposity in metabolic disease. *Nat. Commun.* **12**, 2887 (2021).
96. Notaras, M. et al. Neurodevelopmental signatures of narcotic and neuropsychiatric risk factors in 3D human-derived forebrain organoids. *Mol. psychiatry* **26**, 7760–7783 (2021).
97. Tham, Y. K. et al. Estrogen receptor alpha deficiency in cardiomyocytes reprograms the heart-derived extracellular vesicle proteome and induces obesity in female mice. *Nat. Cardiovascular Res.* **2**, 268–289 (2023).
98. Rai, A., Fang, H., Claridge, B., Simpson, R. J. & Greening, D. W. Proteomic dissection of large extracellular vesicle surfaceome unravels interactive surface platform. *J. Extracell. vesicles* **10**, e12164 (2021).
99. Lozano, J. et al. Scalable generation of nanovesicles from human-induced pluripotent stem cells for cardiac repair. *Int. J. Mol. Sci.* **23**, 14334 (2022).



100. Tyanova, S., Temu, T. & Cox, J. The MaxQuant computational platform for mass spectrometry-based shotgun proteomics. *Nat. Protoc.* **11**, 2301–2319 (2016).
101. Kall, L., Canterbury, J. D., Weston, J., Noble, W. S. & MacCoss, M. J. Semi-supervised learning for peptide identification from shotgun proteomics datasets. *Nat. Methods* **4**, 923–925 (2007).
102. Tyanova, S. & Cox, J. Perseus: a bioinformatics platform for integrative analysis of proteomics data in cancer research. *Methods Mol. Biol. (Clifton, NJ)* **1711**, 133–148 (2018).

## Acknowledgements

We acknowledge funding support from the Victorian State Government OIS program to Baker Heart & Diabetes Institute (BHDI). These studies were supported by funding from the BHDI Obesity & Lipid Program, as well as fellowship support to BGD and ACC from the National Heart Foundation of Australia (101789 and 105631, respectively), and to BGD from the NHMRC (Investigator Grant 2016530). LEF acknowledges support from the Mito Foundation and the NHMRC (Investigator Grant 2010149). We thank members of the MMA, LMCD, Metabolomics, and Molecular Proteomics laboratories at BHDI for their contributions. We also acknowledge support from Prof Mark A. Febbraio (BHDI & Monash Institute of Pharmaceutical Sciences) in generating the floxed mouse, and guidance and resources from Michael T Ryan (Monash University). We are grateful for platform support from the Monash Histology Platform, Department of Anatomy and Developmental Biology at Monash University, Natalia Carvajal and Andrew Perkins from the Centre of Genomic Medicine at the Alfred Hospital Monash University, The La Trobe University Proteomics and Metabolomics Platform, and the University of Melbourne Mass Spectrometry and Proteomics Facility. We also thank A/Prof Peter Crouch from the School of Biomedical Sciences, University of Melbourne, Australia for providing skeletal muscle samples from the global PolG Mutator Model. Various figure panels were created using BioRender.com, with all such figure content sublicensed accordingly.

## Author contributions

B.G.D. conceived the study and co-designed the experiments with D.C.H., S.T.B. and E.J.K. B.G.D. and D.C.H. conceived and generated the PolG floxed mouse model. B.G.D., S.T.B. & E.J.K. wrote the manuscript. S.T.B., E.J.K., A.Z., A.W.J., S.M.W., Y.L. & C.Y. performed animal experiments and phenotyping. B.G.D., S.T.B., E.J.K., S.M.W., C.Y., Y.L., K.H.L., H.A.F., K.H., D.W.G., A.P.N., S.R.C., T.D., S.C., G.R., D.C.H., P.J.M., L.E.F., D.L.R., A.F., N.E.D., D.Pd.S. & A.C.C. analysed data, processed tissue samples, and performed molecular and biochemical experiments. A.C.C., D.W.G., M.I., A.F. & P.J.M. provided reagents, experimental advice, and access to infrastructure and resources. All authors read and approved the manuscript.

## Competing interests

BGD, STB and DCH together with the Baker Heart & Diabetes Institute declare they are pursuing protection of intellectual property (IP) around the use of proprietary folate cycle metabolite derivatives as therapeutics for mitochondrial diseases, and other degenerative conditions in which 1C-metabolism and the ISR are perturbed. All other authors declare no conflict of interest.

## Additional information

**Supplementary information** The online version contains supplementary material available at <https://doi.org/10.1038/s41467-025-57299-3>.

**Correspondence** and requests for materials should be addressed to Brian G. Drew.

**Peer review information** *Nature Communications* thanks the anonymous reviewers for their contribution to the peer review of this work. A peer review file is available.

**Reprints and permissions information** is available at <http://www.nature.com/reprints>

**Publisher's note** Springer Nature remains neutral with regard to jurisdictional claims in published maps and institutional affiliations.

**Open Access** This article is licensed under a Creative Commons Attribution-NonCommercial-NoDerivatives 4.0 International License, which permits any non-commercial use, sharing, distribution and reproduction in any medium or format, as long as you give appropriate credit to the original author(s) and the source, provide a link to the Creative Commons licence, and indicate if you modified the licensed material. You do not have permission under this licence to share adapted material derived from this article or parts of it. The images or other third party material in this article are included in the article's Creative Commons licence, unless indicated otherwise in a credit line to the material. If material is not included in the article's Creative Commons licence and your intended use is not permitted by statutory regulation or exceeds the permitted use, you will need to obtain permission directly from the copyright holder. To view a copy of this licence, visit <http://creativecommons.org/licenses/by-nc-nd/4.0/>.

© The Author(s) 2025

<sup>1</sup>Baker Heart & Diabetes Institute, Melbourne, Australia. <sup>2</sup>Baker Department of Cardiometabolic Health, University of Melbourne, Melbourne, Australia. <sup>3</sup>School of Translational Medicine, Monash University, Melbourne, Australia. <sup>4</sup>Biochemistry and Molecular Biology, Monash University, Melbourne, Australia. <sup>5</sup>Baker Department of Cardiovascular Research Translation and Implementation, La Trobe University, Melbourne, Australia. <sup>6</sup>Monash Ramaciotti Centre for Cryo Electron Microscopy, Monash University, Melbourne, Australia. <sup>7</sup>Metabolomics Australia, Bio21, Parkville, Australia. <sup>8</sup>ARC Centre of Excellence in Synthetic Biology, QEII Medical Centre, Western Australia, Nedlands, Australia. <sup>9</sup>Telethon Kids Institute, Northern Entrance, Perth Children's Hospital, 15 Hospital Avenue, Western Australia, Nedlands, Australia. <sup>10</sup>School of Health Sciences, University of Tasmania, Launceston, Australia. <sup>11</sup>These authors contributed equally: Simon T. Bond, Emily J. King. ✉ e-mail: [brian.drew@baker.edu.au](mailto:brian.drew@baker.edu.au)